

## REPORT DOCUMENTATION PAGE

AFRL-SR-BL-TR-01-

The public reporting burden for this collection of information is estimated to average 1 hour per response, including the gathering and maintaining the data needed, and completing and reviewing the collection of information. Send comments of information, including suggestions for reducing the burden, to Department of Defense, Washington Headquarters (0704-0188), 1215 Jefferson Davis Highway, Suite 1204, Arlington, VA 22202-4302. Respondents should be aware that notwithstanding any other provision of law, no person shall be subject to any penalty for failing to comply with a collection of information if it does not display a currently valid OMB control number.

PLEASE DO NOT RETURN YOUR FORM TO THE ABOVE ADDRESS.

1. REPORT DATE (DD-MM-YYYY)		2. REPORT TYPE FINAL REPORT		3. DATES COVERED (From - To) 11/15/1998 - 10/14/2000	
4. TITLE AND SUBTITLE  "Real-Time Predictive Flutter Analysis and Continuous Parameter Identification of Accelerating Aircraft"				5a. CONTRACT NUMBER F49620-99-1-0037	
				5b. GRANT NUMBER	
				5c. PROGRAM ELEMENT NUMBER	
6. AUTHOR(S)  Charbel Farhat				5d. PROJECT NUMBER	
				5e. TASK NUMBER	
				5f. WORK UNIT NUMBER	
7. PERFORMING ORGANIZATION NAME(S) AND ADDRESS(ES) Department of Aerospace Engineering Sciences Center for Space Structures and Controls University of Colorado at Boulder Boulder, CO 80309-0429				8. PERFORMING ORGANIZATION REPORT NUMBER 153-0568	
9. SPONSORING/MONITORING AGENCY NAME(S) AND ADDRESS(ES) AFOSR 801 North Randolph Street Rm 732 Arlington, VA 22203-1977				10. SPONSOR/MONITOR'S ACRONYM(S)	
				11. SPONSOR/MONITOR'S REPORT NUMBER(S)  AIR FORCE OFFICE OF SCIENTIFIC RESEARCH (AFOSR) NOTICE OF TRANSMITTAL DTIC. THIS TECHNICAL REPORT HAS BEEN REVIEWED AND IS APPROVED FOR PUBLIC RELEASE LAW AFR 190-12. DISTRIBUTION IS UNLIMITED.	
12. DISTRIBUTION/AVAILABILITY STATEMENT  Approved for public release. Distribution unlimited					
13. SUPPLEMENTARY NOTES					
14. ABSTRACT  See Attached					
15. SUBJECT TERMS					
16. SECURITY CLASSIFICATION OF:			17. LIMITATION OF ABSTRACT	18. NUMBER OF PAGES	19a. NAME OF RESPONSIBLE PERSON
a. REPORT	b. ABSTRACT	c. THIS PAGE			19b. TELEPHONE NUMBER (Include area code)

**AIR FORCE OFFICE OF SCIENTIFIC RESEARCH  
GRANT F49620-99-1-0037  
Final Report - January 2001**

**CHARBEL FARHAT**

*Department of Aerospace Engineering Sciences  
Center for Space Structures and Controls  
University of Colorado at Boulder  
Boulder, CO 80309-0429*

**SUMMARY**

This is a four-part final report on the research supported by the Air Force Office of Scientific Research Center under Grant F49620-99-1-0037, entitled **Real Time Predictive Flutter Analysis and Continuous Parameter Identification of Accelerating Aircraft**.

**1. Motivations and research objectives**

Flutter clearance, which is part of any new aircraft or fighter weapon system development, is a lengthy and tedious process from both computational and flight testing viewpoints. An automated approach to flutter clearance that increases flight safety and reduces flight hours requires as a stepping stone the development of a real time flutter prediction capability. Such a fast analysis tool can be designed if the coupled fluid/structure aeroelastic system is represented by a simplified mathematical model that can be quickly adapted to changes in flight atmospheric conditions, aircraft mass distribution (weapon systems), fuel loading, and Mach number, and if the current parallel processing technology is exploited.

Furthermore, flight testing is always required to establish the flutter envelope of an aircraft. The traditional method for determining such an envelope uses test data extracted from the vibration response of the aircraft at fixed flight conditions. The aircraft is first trimmed to a specific flight condition (Mach number and dynamic pressure), then its aeroelastic response is deliberately excited by applying an input to a flight control surface. The frequency and damping of the excited aeroelastic response are typically extracted from

20010402 107

the vibration data. By repeating this test at many flight conditions, the flutter envelope can be determined. Such a traditional approach requires that the aeroelastic response be measured at many different flight conditions. This often requires a large number of flight test hours, a process which not only costs money but also exposes test pilots to proportionately increased risk. However, this test procedure can be expedited if data collected from continuously varying flight conditions can be used to extract the needed flutter damping and frequency values from an accelerating flight profile. In that case, it may be possible to greatly reduce the number of flight hours required for establishing the flutter envelope.

The Air Force Flight Test Center at the Edwards Air Force Base (AFB) has expressed great interest in the above two problems, and therefore we have proposed to conduct a three-year research effort in real time flutter analysis, and the continuous parameter identification of an accelerating aircraft. More specifically, we have proposed to develop a simplified flutter analysis method that can be run real time to provide predictive frequency and damping values for maneuvers as flown. The enabling technology of such a real time flutter analysis capability is a formulation of the aeroelastic problem that allows, among other things, partial pre-solutions and the usage of parallel processing. We have reported on this research activity during the first year of support.

We have also proposed to develop a parameter identification technique that can be used to extract frequency and damping values of an aircraft that is continuously accelerating. This technique should reduce both the cost and risk involved in determining the flutter envelopes of fighters. Here, we report on this effort which has been conducted during the last two years in collaboration with the researchers and engineers of the Air Force Flight Test Center at the Edwards AFB.

## **2. Major accomplishments during the last two years of support**

We have determined that two fundamental issues must be addressed before a method for the continuous parametric identification of an accelerating aircraft can be developed. The first issue deals with how the aeroelastic properties of an aircraft can be affected by a constant acceleration in a level flight or during maneuvering. In particular, is it possible to relate in a simple way the aeroelastic parameters measured in an accelerated flight to those measured in stabilized flight conditions? The second issue is related to the fact that most if not all identification methods used in practice implicitly assume that the given aeroelastic system is linear and non-varying in time. Whether these methods can still be used to analyze accelerated flight data, or whether new methods are required for this purpose was an open question.

During the last two years of funding, we have addressed important aspects of the above two issues by performing appropriate analytical studies and CFD based numerical simulations. More specifically, we have first considered a typical NACA 0012 wing section, and investigated the effects of horizontal and vertical accelerations on the aeroelastic response of this system. We have shown analytically that accelerating the wing section introduces additional inertia forces and modifies the torsional stiffness of the aeroelastic

system by a negligible quantity. Next, we have developed a procedure for extracting the frequencies and damping coefficients of an aeroelastic system from time history data of an accelerated flight profile. This procedure is based on a modification of the ERA algorithm, and its interaction with a windowing concept where the Mach number is assumed to be constant in each window. In order to validate this new procedure, we have upgraded our computational aeroelasticity capability to handle accelerated flight, which was by itself an interesting and rewarding research. We have simulated both cases of stabilized flight conditions and accelerated flight. We have compared the generated results and formulated conclusions regarding the theoretical and practical feasibilities of extracting the flutter envelope of an aircraft from an accelerated flight data. These conclusions essentially highlighted the significant potential of this new concept of flight testing. Motivated by our success for the NACA0012 airfoil, we have repeated our simulations of the continuous parameter identification of an accelerating aeroelastic system for a typical F-16 wing section. We have designed this wing section from geometrical and structural data obtained from the Edwards Air Force Base. We have simulated the continuous parameter identification for the F-16 Block 40 typical wing section in accelerated flights with up to 0.05 Mach per second and for flight regimes extending from subsonic to supersonic. We have shown that the aeroelastic parameters identified in accelerated level flight at a given altitude are almost identical to those obtained in stabilized flight conditions, which justifies the proposed new concept of flight testing. However, we could not match perfectly the results of the numerical simulations using the typical wing section with those of the actual test of the F-16 Block 40, particularly for damping. This was because the available test data is for a loaded wing, whereas our typical wing model was derived from a clean wing model, and because the typical wing section approach is valid only for uniform, straight and high aspect ratio wings. All these developments and findings are described in the attached paper "Expanding a Flutter Envelope Using Accelerated Flight Data: Application to an F-16 Fighter Configuration".

Next, we have designed a three-dimensional F-16 Block 40 aeroelastic model using two incomplete finite element structural models acquired from Lockheed-Martin: (1) a static model which does not contain the mass distribution, and (2) a linear "fish-stick" dynamic model which contains the needed mass information but which is not adequate for stress analysis. Using this model, we have obtained numerical results for the F-16 Block 40 that agreed amazingly well with the flight test data. This latest development is described in details in the attached paper "Application of a Three-Field Nonlinear Fluid-Structure Formulation to the Prediction of the Aeroelastic Parameters of an F-16 Fighter".

### **3. Impact on the state-of-the-art of flight testing**

Motivated by the results we have generated under this Grant, the Air Force Test Pilot School performed on May 15-16, 2000, two suites of accelerated flight tests designed by the Principal Investigator and his collaborators at Edwards. The first series of tests was for a clean (no stores) F-16 configuration, and the second for an F-16 configuration known to cause Limit Cycle Oscillations (LCO). In both cases, the flight test team was



able to accomplish the set objectives using 2.5 times less sorties than when using the classical stabilized flight testing approach, which demonstrates the potential impact of our accomplishments on the flight testing technology.

#### 4. Publications that have resulted from the last two years of support

1. C. Farhat, P. Geuzaine and G. Brown, "Application of a Three-Field Nonlinear Fluid-Structure Formulation to the Prediction of the Aeroelastic Parameters of an F-16 Fighter," *Computers and Fluids*, (submitted for publication)
2. C. Degand and C. Farhat, "A Three-Dimensional Torsional Spring Analogy Method for Unstructured Dynamic Meshes," *Computers and Structures*, (submitted for publication)
3. C. Farhat, K. Pierson and C. Degand, "Multidisciplinary Simulation of the Maneuvering of an Aircraft," *Engineering with Computers*, (in press)
4. M. Lesoinne and C. Farhat, "A CFD Based Method for Solving Aeroelastic Eigenproblems in the Subsonic, Transonic, and Supersonic Regimes," *AIAA Journal of Aircraft*, (in press)
5. M. Lesoinne, M. Sarkis, U. Hetmaniuk and C. Farhat, "A Linearized Method For the Frequency Analysis of Three-Dimensional Fluid/Structure Interaction Problems in all Flow Regimes," *Computer Methods in Applied Mechanics and Engineering*, (in press)
6. C. Felippa, K. C. Park and C. Farhat, "Partitioned Analysis of Coupled Mechanical Systems," *Computer Methods in Applied Mechanics and Engineering*, (in press)
7. S. Piperno and C. Farhat, "Design of Efficient Partitioned Procedures for the Transient Solution of Aeroelastic Problems," *La Revue Européenne des Eléments Finis*, Vol. 9, No. 6/7, pp. 655-680 (2000)
8. C. Farhat and M. Lesoinne, "Two Efficient Staggered Procedures for the Serial and Parallel Solution of Three-Dimensional Nonlinear Transient Aeroelastic Problems," *Computer Methods in Applied Mechanics and Engineering*, Vol. 182, pp. 499-516 (2000)
9. C. Farhat, C. Harris and D. Rixen, "Expanding a Flutter Envelope Using Accelerated Flight Data: Application to an F-16 Fighter Configuration," *AIAA Paper 2000-1702, 41st AIAA/ASME/ASCE/AHS/ASC Structures, Structural Dynamics, and Materials Conference*, Atlanta, GA, April 3-6 (2000)
10. D. Rixen and C. Farhat, "A Computational Methodology for the Simulation of Flow Problems Past Accelerating Rigid and Flexible Obstacles," (abstract), *Fifth U.S. National Congress on Computational Mechanics*, Boulder, Colorado, August 4-6 (1999)
11. D. Rixen, C. Farhat and L. D. Peterson, "Simulation of the Continuous Parametric Identification of an Accelerating Aeroelastic System," *AIAA Paper 99-0797, 37th Aerospace Sciences Meeting and Exhibit*, Reno, Nevada, January 11-14 (1999)

# Expanding a Flutter Envelope Using Accelerated Flight Data: Application to an F-16 Fighter Configuration

† C. Farhat \*, † C. Harris, and ‡ D. J. Rixen †

† Department of Aerospace Engineering Sciences

and Center for Aerospace Structures

University of Colorado, Boulder, CO 80309-0429

‡ LTAS-Dynamics of Structures

University of Liège, Belgium

Using both simple analytical investigations and complex numerical simulations, we show that typical accelerations of an aircraft do not affect significantly its aeroelastic parameters. This suggests that flutter testing could be performed in accelerated flight, thereby reducing the cost and risk involved in determining the flutter envelopes of fighters. We illustrate this concept with numerical simulations for an F-16 fighter configuration and compare the obtained results with flight test data.

## 1 Introduction

Flight testing is always required for establishing the flutter boundary of an aircraft. The traditional method for determining a flutter envelope uses data extracted from the vibration response of the aircraft at stabilized flight conditions. Typically, the aircraft is first trimmed to a specific Mach number and dynamic pressure, then its aeroelastic response is excited by applying an input to one of its control surfaces. The frequency and damping of this response are then extracted from the vibration data. By repeating this test at several different stabilized flight conditions, the flutter envelope is determined.

The traditional testing approach summarized above implies a relatively large number of flight test hours, a process which is not only expensive, but also exposes test pilots to increased risks. One way to expedite this test procedure is to develop a method for expanding the flutter envelope of an aircraft which can use data collected from continuously varying flight conditions. By extracting the critical damping and frequency values from an accelerating flight profile, it may be possible to substantially reduce the number of flight test hours required for establishing the flutter

envelope of an aircraft. However, two fundamental issues must be addressed before a method for the continuous parametric identification of an accelerating aircraft can be developed.

The first issue deals with determining how the aeroelastic properties of an aircraft can be affected by a constant acceleration in a level flight or during a maneuver. In particular, it is important to figure out whether it is possible to relate in a simple manner the aeroelastic parameters measured in an accelerated flight to those measured in stabilized flight conditions. To the best of our knowledge, this issue has not been addressed in depth in the literature [1].

The second issue is related to the fact that most if not all identification methods used in practice implicitly assume that the given aeroelastic system is linear and time-invariant. Whether these methods can still be used to analyze accelerated flight data, or whether new methods are required for this purpose remains an open question.

In this paper, our main objective is to address some preliminary aspects of the two issues raised above by performing both simple analytical investigations, and complex numerical simulations. For this purpose, we first derive the equations of motion of a typical wing section set into an accelerated motion, and assess the

\*Professor, AIAA Fellow

†FNRS Fellow, AIAA Professional Member

Copyright © 2000 by C. Farhat. Published by the American Institute of Aeronautics and Astronautics, Inc. with permission.

effect of the acceleration on the stiffness of this system. This allows us to address the first issue raised above. Next, we overview a computational framework for the simulation of the transient aeroelastic response of an accelerating structure, and describe a "windowing" approach for identifying the parameters of a time-varying system. In order to address the second issue raised in this paper, we perform several numerical simulations for an F-16 aeroelastic configuration. More specifically, we determine a first damping vs. Mach number curve by performing a series of aeroelastic computations corresponding to a sequence of stabilized flight conditions. Then, we perform a *single* simulation of the aeroelastic response of the F-16 airframe to perturbations generated during an accelerated flight. We process the continuous signal generated by this simulation by our window-based identification method, and extract a second damping vs. Mach number curve for this aircraft. We compare both simulated curves, contrast them with flight test data, and offer preliminary conclusions regarding the feasibility of extracting the flutter envelope of an aircraft from accelerated flight test data.

## 2 Aeroelastic response of a typical wing section immersed in an accelerating flow

### 2.1 Discrete structural equations of motion

In the absence of any acceleration, the equations of motion of the typical wing section shown in Fig. 1 can be written as [1]

$$m\ddot{h} + S_\theta\ddot{\theta} + K_h h = Q_h \quad (1)$$

$$S_\theta\ddot{h} + I_\theta\ddot{\theta} + K_\theta\theta = Q_\theta \quad (2)$$

where  $m$  is the total mass per unit span of the wing,  $h$  and  $\theta$  are the bending and torsional degrees of freedom (d.o.f.) of the wing section,  $S_\theta = m(x_G - x_C)$  and  $I_\theta$  are its static and polar moments of inertia about the elastic axis,  $G$  and  $C$  designate its center of gravity and elastic center,  $K_h$  and  $K_\theta$  are the bending

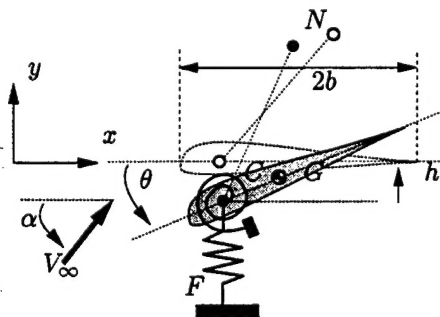


Fig. 1 A typical wing section: elastic center (C), center of gravity (G), fuselage (F), angle of attack ( $\alpha$ ), free-stream velocity ( $V_\infty$ ), a typical point in the flow domain (N)

and torsional stiffness coefficients, and  $Q_h$  and  $Q_\theta$  are the aerodynamic resultant force and moment acting on this section.

Let  $F$  denote a fixed point on the fuselage of the aircraft whose typical wing section is shown in Fig. 1. If the aircraft accelerates and  $\theta$  remains small during the flight, the dynamic equations of equilibrium of the typical wing section become

$$m\ddot{h} + S_\theta\ddot{\theta} + K_h h = Q_h^* \quad (3)$$

$$S_\theta\ddot{h} + I_\theta\ddot{\theta} + K_\theta^* \theta = Q_\theta^* \quad (4)$$

where

$$K_\theta^* = K_\theta - m\gamma_{F_x}(x_G^0 - x_C^0) - m\gamma_{F_y}(y_G^0 - y_C^0) \quad (5)$$

$$Q_h^* = Q_h - m\gamma_{F_y} \quad (6)$$

$$Q_\theta^* = Q_\theta + m\gamma_{F_x}(y_G^0 - y_C^0) - m\gamma_{F_y}(x_G^0 - x_C^0) \quad (7)$$

$\gamma_{F_x}$  and  $\gamma_{F_y}$  are the horizontal and vertical components of the acceleration field, respectively, and the superscript 0 is used to designate the value at time  $t = 0$ . Note that a positive  $\gamma_{F_x}$  corresponds to a deceleration of the wing (see Fig. 1).

From Eq. (6) above, it follows that accelerating the wing section introduces not only additional inertia forces, but also modifies the torsional stiffness of the wing section. However, the reader can check that for level accelerated flight (i.e.  $\gamma_{F_y} = 0$ ) and for most if not all aircraft configurations, the quantity  $m\gamma_{F_x}(x_G^0 - x_C^0)$  is in general negligible compared to  $K_\theta$ . For this reason, we reasonably argue that for all practical purposes,  $K_\theta^* \approx K_\theta$ . Since all other coefficients of the left hand-side of Eqs. (3,4) are not affected by the aircraft acceleration, we conclude that, at least for an accelerated level flight, the aeroelastic parameters (i.e. frequency and damping values) of a typical wing section are the same as for stabilized flight conditions.

In all numerical simulations that we discuss later in this paper, we time-integrate Eqs. (3,4) by the mid-point rule (or Newmark method with  $\beta = 1/4$  and  $\gamma = 1/2$ ).

### 2.2 Discrete fluid equations of motion

The complete description of the typical wing section introduced above requires the evaluation of the aerodynamic resulting force and moment,  $Q_h$  and  $Q_\theta$ . Rather than adopting a linear flow theory whose limitations are well-known, we choose for this purpose to model the fluid by the Euler equations. More specifically, we rely on the Arbitrary Lagrangian Eulerian (ALE) form [2,3] of the Euler equations in order to

handle the vibrations of the airfoil and its acceleration.

Let  $\Omega(t) \subset \mathcal{R}^2$  be the flow domain surrounding the airfoil of the typical wing section, and  $\Gamma(t)$  be its moving boundary. We introduce a mapping function between  $\Omega(t)$  where time is denoted by  $t$  and a grid point's coordinates by  $x$ , and a reference configuration  $\Omega(0)$  where time is denoted by  $\tau$  and a grid point's coordinates by  $\xi$ , as follows

$$x = x(\xi, \tau); \quad t = \tau \quad (8)$$

The ALE conservative form of the Navier-Stokes equations describing viscous flows on dynamic meshes can be written as [3-5]

$$\frac{\partial J\mathcal{W}}{\partial t}|_{\xi} + J\nabla_x \cdot \mathcal{F}^c(\mathcal{W}, \dot{x}) = 0 \quad (9)$$

$$\mathcal{F}^c(\mathcal{W}, \dot{x}) = \mathcal{F}(\mathcal{W}) - \dot{x}\mathcal{W} \quad (10)$$

where a dot superscript designates a time derivative,  $J = \det(dx/d\xi)$ ,  $\dot{x} = \frac{\partial x}{\partial \tau}|_{\xi}$  is the velocity of the dynamic fluid mesh,  $\mathcal{W}$  is the fluid state vector (conservative variables), and  $\mathcal{F}^c$  denotes the ALE convective fluxes.

We semi-discretize Eq. (9) on a triangulation from which we derive a dual mesh defined by time-dependent control volumes or cells  $C_i(t)$ . We resolve the ALE convective fluxes by a suitable Riemann solver [6-9]. The resulting semi-discrete equation of equilibrium of the fluid is

$$\frac{d}{dt}(A_i W_i) + F_i(W, X, \dot{X}) = 0 \quad (11)$$

where  $A_i = \int_{C_i(t)} d_x \Omega$ ,  $W_i$  denotes the average value of  $\mathcal{W}$  over the cell  $C_i(t)$ ,  $F_i$  denotes the semi-discrete ALE convective flux,  $W$  is the vector formed by the collection of  $W_i$ , and  $X$  is the vector of time-dependent grid point positions. Various expressions of the flux approximation  $F_i(W, X, \dot{X})$  can be found in [6-9].

We time-integrate the semi-discrete equations of flow motion (11) on dynamic meshes using the generalized second-order implicit backward difference scheme developed in [10, 11]. This scheme satisfies the second-order discrete geometric conservation law, and retains second-order time-accuracy on moving grids [10, 11]. It can be written in compact form as follows

$$\alpha_{n+1} A_i^{n+1} W_i^{n+1} + \alpha_n A_i^n W_i^n + \alpha_{n-1} A_i^{n-1} W_i^{n-1} + \Delta t^n F_i(W^{n+1}, X_{avg}^{n+1}, \dot{X}_{avg}^{n+1}) = 0 \quad (12)$$

where  $A_i^n = A_i(X^n)$ ,  $X_{avg}^{n+1}$  and  $\dot{X}_{avg}^{n+1}$  are the following averaged position and velocity of the fluid moving mesh

$$\begin{aligned} X_{avg}^{n+1} &= \alpha_{n+1} \left( \frac{X^n + X^{n+1}}{2} \right) - \frac{\alpha_{n-1}}{\zeta} \left( \frac{X^{n-1} + X^n}{2} \right) \\ \dot{X}_{avg}^{n+1} &= \alpha_{n+1} \left( \frac{X^{n+1} - X^n}{\Delta t^n} \right) - \frac{\alpha_{n-1}}{\zeta} \left( \frac{X^n - X^{n-1}}{\Delta t^{n-1}} \right) \end{aligned} \quad (13)$$

$\alpha_{n-1}$ ,  $\alpha_n$ , and  $\alpha_{n+1}$  are time-dependent because a variable time-step  $\Delta t^n$  is employed and are given by

$$\begin{aligned} \zeta &= \frac{\Delta t^n}{\Delta t^{n-1}}, \quad \alpha_{n-1} = \frac{\zeta^2}{1 + \zeta} \\ \alpha_n &= -1 - \zeta, \quad \alpha_{n+1} = \frac{1 + 2\zeta}{1 + \zeta} \end{aligned} \quad (14)$$

It remains to specify how  $X^n$ , the vector position of the fluid grid points, is updated at each time-station  $t^n$ .

For this purpose, we first note that for a typical wing section problem, the simplest strategy for updating the position of the fluid mesh is to move it rigidly with the airfoil. Then, we also note that the motion of the airfoil is completely determined by the motion of the fuselage point  $F$ , and the vibrations of the bending and torsional d.o.f.  $h$  and  $\theta$ . It follows that at each time-station  $t^n$ , the position of any fluid grid point  $N$  (see Fig. 1) is given by

$$\begin{aligned} x_N^n &= x_F^n + (x_N^0 - x_F^0) \cos \theta^n \\ &\quad - (y_N^0 - y_F^0) \sin \theta^n \\ y_N^n &= y_F^n + h^n + (y_N^0 - y_F^0) \cos \theta^n \\ &\quad + (x_N^0 - x_F^0) \sin \theta^n \end{aligned} \quad (15)$$

where  $h^n$  and  $\theta^n$  are determined by solving the coupled fluid/structure equations of motion (3,4,11), and the instantaneous position  $(x_F^n, y_F^n)$  of the fuselage point  $F$  is deduced from the specified acceleration of the aircraft. For example, for a constant acceleration, the instantaneous position of the point  $F$  is given by

$$\begin{aligned} x_F^n &= \frac{\gamma_{F_x}}{2} t^{n2} + x_F^0 \\ y_F^n &= \frac{\gamma_{F_y}}{2} t^{n2} + y_F^0 \end{aligned} \quad (16)$$

Hence, the acceleration of the typical wing section is transmitted to the fluid by Eqs. (16), and accounted for by the additional convection term  $\dot{x}\mathcal{W}$  that characterizes the ALE form (9) of the flow equations.

**Remark.** At the first glance, the reader may think that Eqs. (16) are missing the terms  $V_{\infty_x} t^n$  and  $V_{\infty_y} t^n$ , where  $V_{\infty}$  is the free-stream velocity. However, these terms are not missing. They are automatically taken into account by the initial conditions of the CFD simulation through the specified free-stream Mach number  $M_{\infty}$ .

## 2.3 Solution of the coupled fluid/structure equations of motion

Throughout this paper, we solve the coupled fluid/structure discrete equations of motion by the second-order time-accurate staggered and subiteration free algorithm described in [12]. As stated earlier, we equip this staggered algorithm with the midpoint rule as a structural time-integrator, and the generalized second-order implicit backward difference scheme (12) developed in [10,11] as a flow time-integrator.

## 3 System identification using the ERA

### 3.1 Identification on a window-by-window basis

Depending on several factors among which the flow regime, an aeroelastic system can behave linearly or non-linearly. This raises a first albeit minor concern as to the applicability of several popular signal processing techniques to the identification of the aeroelastic parameters of an aircraft, or a typical wing section, particularly in the transonic regime. Furthermore, an accelerated aeroelastic system is also a time-varying system. This is essentially because the mass, damping, and stiffness properties of the "wet" structure are influenced by the free-stream velocity  $V_\infty$  of this structure, and  $V_\infty$  varies with time during an accelerated flight. This raises a second concern as to the applicability of these signal processing methods to the continuous parametric identification of an accelerating aircraft. Both concerns can be addressed by the windowing approach described below, which is in principle applicable to several identification methods.

First, we note that

- some methods are capable of identifying the frequency and damping coefficient of the lowest mode of a structure using as few as 2 cycles of the response of this structure to an input perturbation.
- for a mode at 10 Hz, 2 cycles correspond to a time interval of 0.2 second.
- at an altitude of 3,000 meters, a level flight acceleration of 0.05 Mach/second corresponds to a horizontal acceleration of 1.6 gs. Such an acceleration is beyond the reach of most if not all aircraft.
- during a time-interval of 0.2 second, the speed of an aircraft accelerating at 0.05 Mach/second varies by 0.01 Mach.
- a 1% variation of a Mach number  $M_\infty$  has a negligible effect on the frequency and damping coefficient of a wet structure cruising at  $M_\infty$ .

From the above observations, we conclude that within a time-window of the order of 0.2 second, an

aeroelastic system with a first wet mode at 10 Hz can be considered for all practical purposes as a time-invariant system. Furthermore, within a window of that size, the aeroelastic response of such a system can be assumed to be linear, as long as the structure itself behaves linearly, which is usually the case for an aircraft excited by an input to a control surface. Hence, we also conclude that at least in principle, it should be possible to expand the flutter envelope of an aircraft using its continuous vibration response to input perturbations during and accelerated flight by applying the following simple procedure

1. locate the time instances at which the Mach numbers of interest are reached by the aircraft.
2. for each Mach number of interest, define a time-window of width equal approximately to 0.2 second or two cycles of the expected lowest frequency.
3. within each time-window, apply a suitable signal processing method to identify the frequency and damping coefficient of the wet structure and associate these with the Mach number for which this window is defined.

The window-based identification approach summarized above can be performed either real-time, or off-line as a signal post-processing. In this work, we choose to base it on the Eigenvalue Realization Algorithm (ERA) [13].

The ERA is an identification method for linear and time-invariant systems. It implicitly assumes that the dynamic response of the given system is sampled at a constant rate. It can handle multi-d.o.f. systems, and is less sensitive to noise than the logarithmic decay method. In order to keep this paper self-contained, we overview next the ERA and its fast implementation FastERA [14,15] which is suitable for real-time processing.

### 3.2 Overview of the ERA

In a linear context, damped structural vibrations are governed by the following equations of dynamic equilibrium

$$M\ddot{q} + D\dot{q} + Kq = f(t) \quad (17)$$

where  $M, D, K$  are respectively the mass, damping and stiffness matrices, and where  $f$  denotes the vector of external loads. The above equations can be re-written in state-space form as follows

$$\begin{cases} \dot{x} = Kx + Bf(t) \\ q = Cx \end{cases} \quad (18)$$



where

$$\begin{aligned} \mathbf{x} &= \begin{bmatrix} \mathbf{q} \\ \dot{\mathbf{q}} \end{bmatrix} \\ \mathbf{K} &= \begin{bmatrix} \mathbf{0} & \mathbf{I} \\ -\mathbf{M}^{-1}\mathbf{K} & -\mathbf{M}^{-1}\mathbf{D} \end{bmatrix} \\ \mathbf{B} &= \begin{bmatrix} \mathbf{0} \\ \mathbf{M}^{-1} \end{bmatrix} \quad \mathbf{C} = \begin{bmatrix} \mathbf{I} & \mathbf{0} \end{bmatrix} \end{aligned} \quad (19)$$

Assuming that initially the structural system is at rest, and that it is excited at  $t = 0$  by an impulse load  $\mathbf{f}(t) = \mathbf{u}_0\delta(t)$  where  $\delta$  denotes the Dirac delta function, the solution of Eq. (18) is

$$\mathbf{q}(t) = \mathbf{C}e^{\mathbf{K}t}\mathbf{B}\mathbf{u}_0 \quad (20)$$

Note that Eq. (20) is also the solution of the problem (18) for  $\mathbf{f}(t) = \mathbf{0}$  and an initial velocity equal to  $\mathbf{M}^{-1}\mathbf{u}_0$ .

For an arbitrary excitation,  $\mathbf{f}(t)$  can be represented by a series of impulses at discrete time-stations  $t_i$  — that is,  $\mathbf{f}(t) = \sum_{i=1}^{\infty} \mathbf{u}_i\delta(t-t_i)$ , in which case the solution of Eq. (18) at time  $t_k$  is given by

$$\begin{aligned} \mathbf{q}_k = \mathbf{q}(t_k) &= \sum_{i=0}^k \mathbf{C}e^{(t_k-t_i)\mathbf{K}}\mathbf{B}\mathbf{u}_i \\ &= \sum_{i=0}^k \mathbf{C}e^{(k-i)\Delta t\mathbf{K}}\mathbf{B}\mathbf{u}_i \end{aligned} \quad (21)$$

where a constant sampling rate  $1/\Delta t$  is assumed so that  $t_k - t_i = (k-i)\Delta t$ .

Let

$$\mathbf{A} = e^{\Delta t\mathbf{K}} \quad (22)$$

Using the above definition of the matrix  $\mathbf{A}$ , Eq. (21) can be re-written as follows

$$\begin{aligned} \mathbf{q}_k &= \sum_{i=0}^k \mathbf{C}\mathbf{A}^{k-i}\mathbf{B}\mathbf{u}_i \\ &= \sum_{i=0}^{k-1} \mathbf{C}\mathbf{A}^{k-i-1}(\mathbf{A}\mathbf{B})\mathbf{u}_i + \mathbf{C}\mathbf{B}\mathbf{u}_k \\ &= \sum_{i=0}^{k-1} (\mathbf{C}\mathbf{A}^{k-i-1}\mathbf{B}\mathbf{u}_i) + \mathbf{G}\mathbf{u}_k \end{aligned} \quad (23)$$

where

$$\mathbf{G} = \mathbf{C}\mathbf{B} \quad (24)$$

Hence,  $\mathbf{q}_k$  is the classical solution of the state-space realization problem for the following linear sampled data system

$$\begin{cases} \mathbf{x}_{k+1} = \mathbf{A}\mathbf{x}_k + \mathbf{B}\mathbf{u}_k \\ \mathbf{q}_k = \mathbf{C}\mathbf{x}_k + \mathbf{G}\mathbf{u}_k \end{cases} \quad (25)$$

where

$$\mathbf{B} = \mathbf{A}\mathbf{B} \quad \mathbf{C} = \mathbf{C} \quad (26)$$

If  $n_{dof}$  denotes the total number of d.o.f. of the computational model described by Eq. (17), but only  $n_{dof}^{mes} < n_{dof}$  d.o.f. are measured, then the matrix  $\mathbf{C}$  can be written as

$$\mathbf{C} = \begin{bmatrix} \mathbf{L} & \mathbf{0} \end{bmatrix} \quad (27)$$

where  $\mathbf{L}$  is an  $n_{dof}^{mes} \times n_{dof}$  Boolean matrix. Hence, in general, the number of state-space variables  $\mathbf{x}_k$  that are considered is  $n_x = 2n_{dof}$ , and the matrix  $\mathbf{A}$  defined in Eq. (22) is an  $n_x \times n_x$  matrix.

In general, the discrete convolution sum (23) is expressed as

$$\mathbf{q}_k = \sum_{i=0}^k \mathcal{M}_{k-i}\mathbf{u}_i \quad (28)$$

where the matrices

$$\mathcal{M}_m = \begin{cases} \mathbf{G} & , m = 0 \\ \mathbf{C}\mathbf{A}^{m-1}\mathbf{B} & , m > 0 \end{cases} \quad (29)$$

are known as the Markov parameters. Hence,  $\mathbf{q}_k$  can be directly related to the load components  $\mathbf{u}_i$  via the the Markov parameters  $\mathcal{M}_i$ .

Let  $\mathbf{z}_s$  and  $\lambda_s = \alpha_s \pm i\omega_s$  denote the complex eigenmodes and eigenfrequencies of the structure defined by

$$\lambda_s^2 \mathbf{M}\mathbf{z}_s + \lambda_s \mathbf{C}\mathbf{z}_s + \mathbf{K}\mathbf{z}_s = \mathbf{0} \quad (30)$$

From Eqs. (19), it follows that the  $\lambda_s$  are also the eigenvalues of  $\mathbf{K}$ , and the eigenvectors of this matrix are

$$\mathbf{y}_s = \begin{bmatrix} \mathbf{z}_s \\ \lambda_s \mathbf{z}_s \end{bmatrix} \quad (31)$$

The ERA exploits the results summarized above as follows. First, it constructs the Markov parameters  $\mathcal{M}_k$  using the input and output data, namely, the impulse loads and measured displacements. Then, it

extracts the matrix  $\mathbf{A}$  from the Markov parameters  $\mathcal{M}_k$  using, for example, the FastERA algorithm described in Section 3.3. Finally, the ERA computes the eigenvalues  $\sigma_s$  and eigenvectors  $\mathbf{a}_s$  of  $\mathbf{A}$  which satisfy

$$\mathbf{A}\mathbf{a}_s = \sigma_s \mathbf{a}_s \quad (32)$$

From Eq. (22), it follows that the sought-after complex modes  $\mathbf{z}_s$ , damping ratios  $\xi_s$ , and frequencies  $\omega_s$  of the given structural system are given by

$$\mathbf{z}_s = \mathbf{C}\mathbf{a}_s \quad (33)$$

$$\xi_s = \frac{1}{\omega_s \Delta t} \operatorname{Re}\{\ln(\sigma_s)\} \quad (34)$$

$$\omega_s = \frac{1}{\Delta t} \operatorname{Im}\{\ln(\sigma_s)\} \quad (35)$$

### 3.3 The FastERA algorithm [14]

In this work, we use the FastERA implementation of the ERA to perform all indentifications. For this reason, we review FastERA in this section and introduce some key variables that appear in the remainder of this paper.

The FastERA method is based on the analysis of the following Hankel matrix that is defined for a data set  $(\mathbf{q}_k, \mathbf{u}_k)$  sampled at  $N$  points in time

$$\mathbf{H}_{qd} = \begin{bmatrix} \mathcal{M}_1 & \mathcal{M}_2 & \cdots & \mathcal{M}_d \\ \mathcal{M}_2 & \mathcal{M}_3 & \cdots & \mathcal{M}_{d+1} \\ \vdots & \vdots & \ddots & \vdots \\ \mathcal{M}_{q+1} & \mathcal{M}_{q+2} & \cdots & \mathcal{M}_{q+d-1} \end{bmatrix} \quad (36)$$

and where  $q$  and  $d$  are such that  $N = q + d$ . From the definition (29) of the Markov parameters, it follows that  $\mathbf{H}_{qd}$  can be decomposed as follows

$$\mathbf{H}_{qd} = \mathbf{V}_q \mathbf{W}_d \quad (37)$$

where

$$\mathbf{V}_q = \begin{bmatrix} \mathbf{C} \\ \mathbf{CA} \\ \vdots \\ \mathbf{CA}^{q-1} \end{bmatrix}, \quad \mathbf{W}_d = \begin{bmatrix} \mathbf{B} & \mathbf{AB} & \cdots & \mathbf{A}^{d-1}\mathbf{B} \end{bmatrix} \quad (38)$$

The  $qn_{dof}^{mes} \times qn_{dof}^{mes}$  matrix  $\mathbf{V}_q$  determines the observability of the system whereas  $\mathbf{W}_d$  is related to its controllability.

The FastERA method starts with the construction of the  $qn_{dof}^{mes} \times qn_{dof}^{mes}$  "square data matrix"

$$\mathbf{J}_q = \mathbf{H}_{qd} \mathbf{H}_{qd}^T = \mathbf{V}_q \mathbf{W}_d \mathbf{W}_d^T \mathbf{V}_q^T \quad (39)$$

For a given set of inputs  $\mathbf{u}_k$  and outputs  $\mathbf{q}_k$ , the choice of state-space variables  $\mathbf{x}$  is not unique. Indeed, the input/output relation is not affected by the change of variable  $\mathbf{x} = \mathbf{T}\tilde{\mathbf{x}}$  which transforms the realization system (25) into

$$\begin{cases} \tilde{\mathbf{x}}_{k+1} = \mathbf{T}^{-1}\mathbf{A}\mathbf{T}\tilde{\mathbf{x}}_k + \mathbf{T}^{-1}\mathbf{B}\mathbf{u}_k \\ \mathbf{q}_k = \mathbf{C}\mathbf{T}\tilde{\mathbf{x}}_k + \mathbf{G}\mathbf{u}_k \end{cases} \quad (40)$$

The controllability factors associated with  $\tilde{\mathbf{x}}$  are

$$\tilde{\mathbf{W}}_d \tilde{\mathbf{W}}_d^T = \mathbf{T}^{-1} \mathbf{W}_d \mathbf{W}_d^T \mathbf{T}^{-T} \quad (41)$$

In particular, choosing  $\mathbf{T} = (\mathbf{W}_d \mathbf{W}_d^T)^{1/2}$  leads to  $\tilde{\mathbf{W}}_d \tilde{\mathbf{W}}_d^T = \mathbf{I}$ . Hence, without any loss of generality, the FastERA algorithm assumes that the state-space variables are chosen so that Eq. (39) simplifies to

$$\mathbf{J}_q = \mathbf{V}_q \mathbf{V}_q^T \quad (42)$$

From Eq. (38), it follows that the first  $(q-1)n_{dof}^{mes}$  rows of  $\mathbf{V}_q$  are given by

$$\mathbf{V}_q^{(1)} = \begin{bmatrix} \mathbf{C} \\ \mathbf{CA} \\ \vdots \\ \mathbf{CA}^{q-2} \end{bmatrix} \quad (43)$$

and the last  $(q-1)n_{dof}^{mes}$  rows of that matrix are given by

$$\mathbf{V}_q^{(2)} = \begin{bmatrix} \mathbf{CA} \\ \vdots \\ \mathbf{CA}^{q-1} \end{bmatrix} = \mathbf{V}_q^{(1)} \mathbf{A} \quad (44)$$

In general, the number of d.o.f.  $n_{dof}$  associated with a system to be identified is unknown *a priori*. Indeed,  $n_{dof}$  is infinite for any continuous system. In practice, the target values for  $n_{dof}^{mes}$  and the corresponding number of state-space variables  $n_x = 2n_{dof}$  are dictated by the complexity of the model to be realized. Once these values are set by the user, the FastERA algorithm computes the  $n_x$  largest eigenvalues  $\kappa_j$  of  $\mathbf{J}_q$  and their corresponding eigenvectors  $\mathbf{p}_j$  in order to build the square root factorization

$$\tilde{\mathbf{J}}_q = \mathbf{P} \operatorname{diag}(\kappa_j) \mathbf{P}^T \quad (45)$$

$$\begin{aligned} &= \left( \mathbf{P} \operatorname{diag}(\kappa_j^{1/2}) \right) \left( \operatorname{diag}(\kappa_j^{1/2}) \mathbf{P}^T \right) \\ &= \tilde{\mathbf{V}}_q \tilde{\mathbf{V}}_q^T \end{aligned} \quad (46)$$

where  $\mathbf{P} = [\mathbf{p}_1 \dots \mathbf{p}_j \dots]$  and  $\tilde{\mathbf{V}}_q = \mathbf{P} \text{diag}(\kappa_j^{1/2})$ . From Eqs. (43,44) applied to  $\tilde{\mathbf{V}}$ , it follows that

$$\mathbf{A} = (\tilde{\mathbf{V}}_q^{(1)})^+ \tilde{\mathbf{V}}_q^{(2)} \quad (47)$$

where  $(\tilde{\mathbf{V}}_q^{(1)})^+$  is the pseudo-inverse of  $\tilde{\mathbf{V}}_q^{(1)}$ .

Hence, the extraction of the  $n_x$  largest eigenpairs of the  $qn_{dof}^{mes} \times qn_{dof}^{mes}$  data matrix  $\mathbf{J}_q$  is the most computationally significant step of the FastERA algorithm. Keeping  $q$  relatively small, say  $q \approx d/5$ , allows FastERA to operate in real time. For further details on this identification method, we refer the reader to [14].

Next, we validate the window-by-window application of the ERA for the identification of the parameters of an accelerating aircraft by a series of numerical simulations designed for an F-16 fighter configuration for which flight test data is available.

#### 4 Simulation of the continuous parametric identification of an F-16 configuration

Here, we focus on a Block 40 version of the F-16 fighter. Because of CPU time limitations, we consider only two-dimensional numerical simulations. Therefore, we report first on the design of a typical wing section model for this aircraft.

##### 4.1 A typical wing section model for the F-16

We start from a detailed finite element structural model of a "clean" right wing of the F-16 Block 40 equipped with a missile launching system at its tip (Fig. 2). Our objective is to construct a two-d.o.f. wing section model that is equivalent to the three-dimensional wing in the following sense

1. it reproduces the first bending and torsion frequencies which are predicted by the three-dimensional finite element model of the wing to be 4.76 Hz and 7.43 Hz, respectively.
2. it reproduces the same bending and torsion modal masses.
3. it reproduces the same vertical displacement at the leading edge of the cross section located at 68% of the distance from the root to the tip of the three-dimensional wing, for both bending and torsion mode shapes, when these are normalized to a unit rotation of the cross section.

When the wing has a large aspect ratio and a small sweep angle, it is commonly suggested to choose the mechanical properties of the typical wing section as to match those of the cross section located at 70% to

75% of the distance from the root to the tip of the three-dimensional wing (for example, see [1] and references 6-1 and 6-2 therein). Nevertheless, we choose in criterion 3 stated above the cross-section located at 68% of the distance from the root to the tip (see Fig. 2) because the F-16 wing is strongly tapered and is rather soft towards its tip.

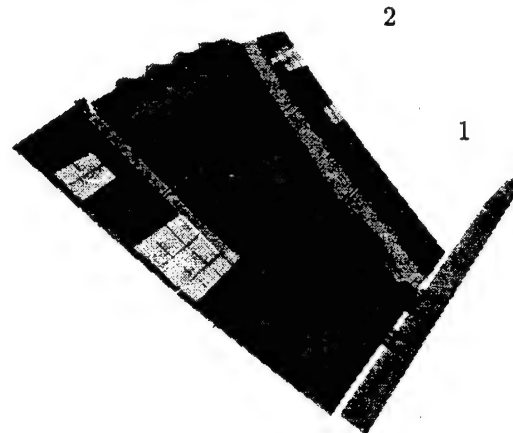
Besides the shape of the airfoil, six parameters define the sought-after typical wing section. These are denoted collectively by  $P_{tw}$ , where the subscript  $tw$  stands for typical wing section, and listed below

$$P_{tw} = \{m, I_\theta, x_G, (x_G - x_C), K_h, K_\theta\}$$

The three criteria stated above for establishing the equivalence between the typical wing section and the three-dimensional wing can be formulated as follows

$$\begin{bmatrix} \Omega_{tw,1}(P_{tw}) \\ \Omega_{tw,2}(P_{tw}) \\ \mu_{tw,1}(P_{tw}) \\ \mu_{tw,2}(P_{tw}) \\ h_{tw,1}^{le}(P_{tw}) \\ h_{tw,2}^{le}(P_{tw}) \end{bmatrix} = \begin{bmatrix} 2\pi \times 4.76 \text{ rad/s} \\ 2\pi \times 7.43 \text{ rad/s} \\ 1.375 \cdot 10^6 \text{ Kg.m}^2 \\ 2.523 \text{ Kg.m}^2 \\ 25.61 \text{ m} \\ 1.017 \text{ m} \end{bmatrix} \quad (48)$$

where  $\Omega$  denotes a frequency, the subscripts 1 and 2 refer to the bending and torsion modes, respectively,  $\mu$  denotes a modal mass, the superscript  $le$  designates the leading edge,  $h^{le} = h + (x^{le} - x_C)(\theta = 1)$  is the vertical displacement at the leading edge of the typical wing section, and all components of the right hand-side of Eq. (48) are obtained from the detailed



1: cross-section chosen for the structural properties  
2: cross-section chosen for the aerodynamic properties

Fig. 2 Three-dimensional detailed finite element model of an F-16 wing

finite element model of the three-dimensional wing. Note that the fact that  $h_{tws,1}^{te} \gg h_{tws,2}^{te}$  suggests that despite the bending/torsion coupling, the first mode of the wing is dominated by bending, while the second one is dominated by torsion.

The constraints (48) lead to a nonlinear system of equations with six unknowns, which we solve by the Nelder-Mead simplex method (function *fminf* in Matlab) to obtain

$$\begin{aligned} m &= 2.05 \cdot 10^3 \text{ Kg} \\ I_\theta &= 2.53 \cdot 10^{-4} \text{ Kg.m}^2 \\ x_G &= 1.128 \text{ m} \\ &\quad (\text{upstream of section at 68\%}) \\ (x_G - x_C) &= 0.0642 \text{ m (G behind C)} \\ K_h &= 2.046 \cdot 10^6 \text{ N/m} \\ K_\theta &= 5.468 \cdot 10^6 \text{ N.m} \end{aligned}$$

Using the above numbers, we find that the modified torsional stiffness (see Eq. 6) for an acceleration as high as 0.05 Mach/second is  $K_\theta^* = 5.471 \cdot 10^6 \text{ N.m}$ . Hence, as expected,  $K_\theta^* \approx K_\theta$ , which supports the conclusion made in Section 2.1 as to the little effect of level flight acceleration on the aeroelastic parameters of a system.

Finally, we assume modal damping ratios of 1.0% and 1.5% for the first and second vibration modes of the typical wing section, respectively.

#### 4.2 The airfoil and the flow computational domain

We choose the airfoil of the typical wing section as that of the cross section located at 45% of the distance between the root and tip of the three-dimensional wing (see Fig. 2), because

- the chord of the airfoil of the typical wing section must be close to the ratio of the wetted area and the wing span.
- because of tapering, most of the lift is generated by the section of the wing that is close to the root, which means that the aerodynamic center of the wing is within that area.

We discretize the flow domain by 18,000 vertices, and ensure a sufficient resolution for shock capturing in the region close to the sharp leading edge (Fig. 3). Because the purpose of the typical section is to represent the entire wing, we multiply each aerodynamic force obtained from a flow computation on this two-dimensional mesh by the span of the wing.

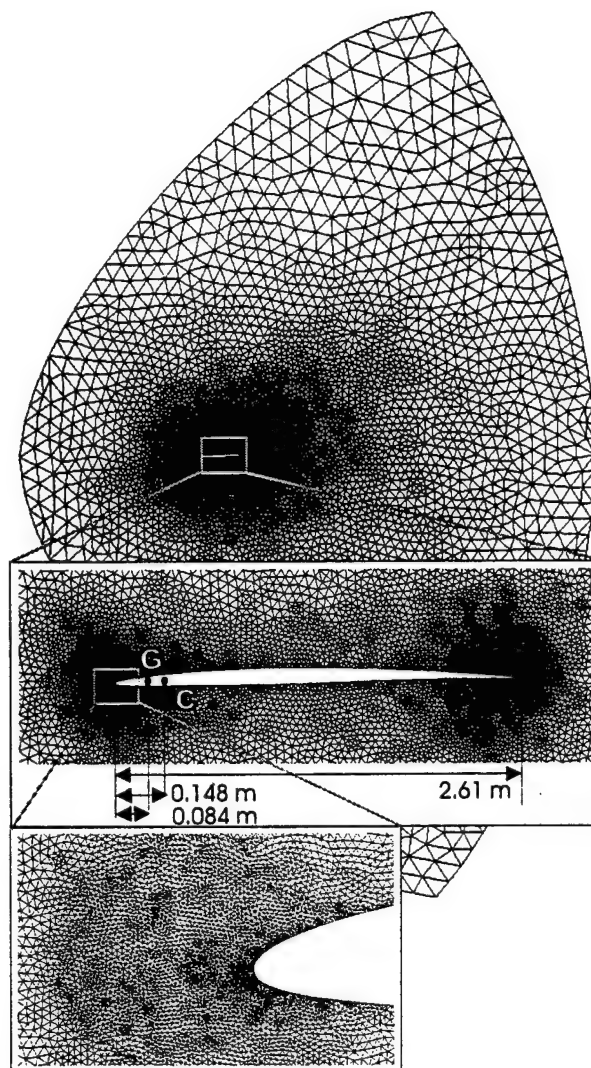


Fig. 3 Discretization of the flow computational domain (F-16 airfoil)

#### 4.3 Aeroelastic numerical simulations

We fix the altitude to 3,000 m, set the angle of attack to 0 degree, and perform first a series of aeroelastic simulations for a sequence of stabilized flight conditions at the following Mach numbers: 0.8, 0.85, 0.875, 0.9, 0.925, 0.95, 1.0, 1.1, 1.2, 1.3 and 1.4. For each Mach number, we start the numerical simulation from a steady-state flow and the following initial conditions for the typical wing section:  $\dot{h}^0 = 0.01 \text{ m/s}$ , and  $\dot{\theta}^0 = 0.2 \text{ rad/s}$ . We report in Fig. 4 and Fig. 5 the predicted transient responses of the structure at  $M_\infty = 0.8$  and  $M_\infty = 1.0$ , respectively. We also include at the top of both figures the iso-Mach contour plots at  $t = 0$ . These figures show that at  $M_\infty = 0.8$ , the aeroelastic vibrations are rapidly damped out. They also show that at  $M_\infty = 0.8$ , both modes of the typical wing section contribute initially to the bending d.o.f.  $h$ , but only one mode of the typical wing section contributes to the history of the torsional d.o.f.  $\theta$ . We conclude that it is the bending mode of

the typical wing section that is rapidly damped out at  $M_\infty = 0.8$ . The history of  $\theta(t)$  graphically depicted in Fig. 5 reveals that flutter or limit cycle oscillations are initiated at  $M_\infty = 1.0$ .

Next, we simulate the aeroelastic response of the typical wing section during a flight accelerated at the rate of 0.05 Mach/second. We remind the reader that such an acceleration is even higher than what an F-16 can achieve in a level flight. We initiate this simulation at  $M_\infty = 0.75$  and excite the structure with the same initial conditions as previously:  $\dot{h}^0 = 0.01$  m/s, and  $\dot{\theta}^0 = 0.2$  rad/s. We report in Fig. 6 the predicted response of the structure. The reader can observe that both modes of the typical wing section contribute to the early response of the  $h$  d.o.f. The significant decrease of the mean value of  $h$  that is noted between Mach 0.8 and Mach 0.95 suggests an important drop in the lift in this Mach region, which, given that the F16 airfoil is unsymmetric, is indicative of the appearance of a shock and reaching the Mach divergence speed. Most importantly, Fig. 6 shows that between Mach 0.85 and Mach 0.95, the vibrations of  $h$  and  $\theta$  become too small to allow a parametric identification. Hence, we conclude that a continuous parametric identification of an aircraft that accelerates across the subsonic, transonic, and supersonic regimes requires systematic re-excitations.

In order to illustrate the effect of re-excitation, we simulate a second accelerated flight where the initial

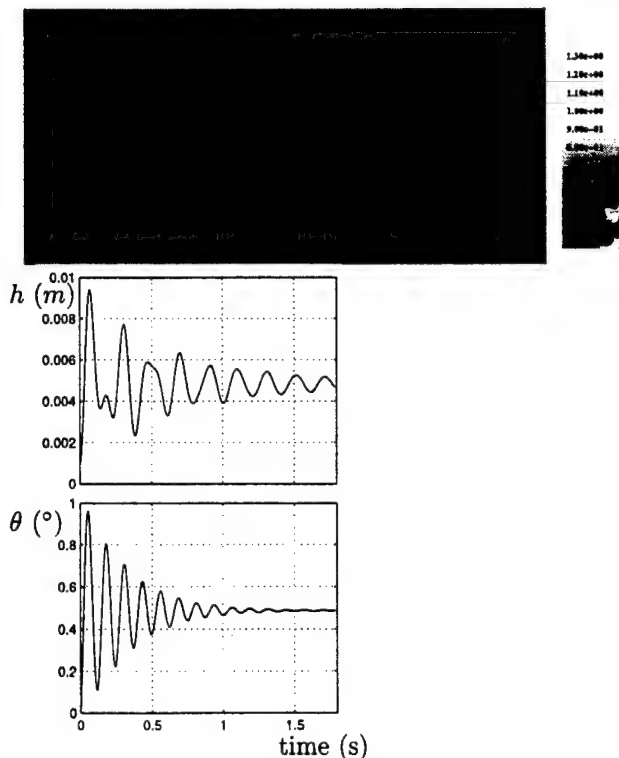


Fig. 4 Transient aeroelastic response for stabilized flight conditions at Mach = 0.80

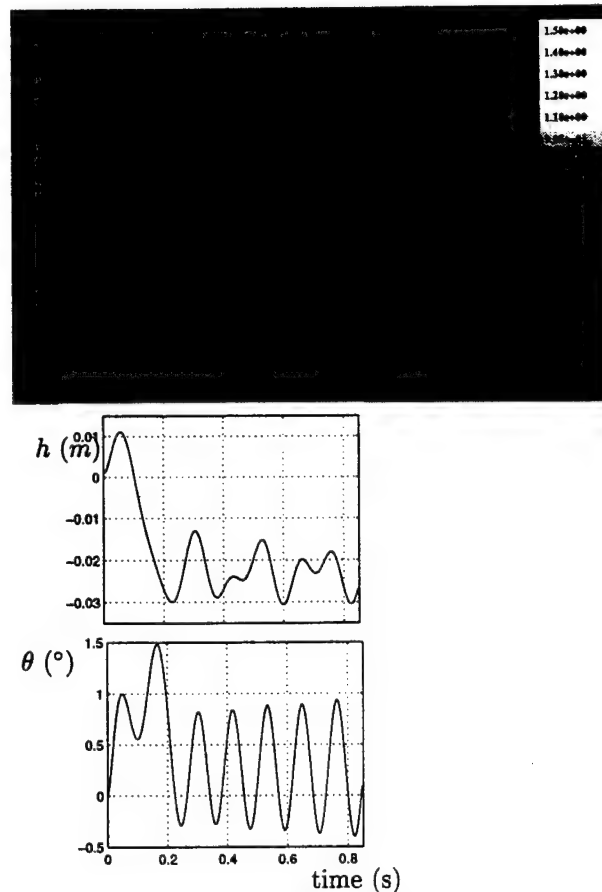


Fig. 5 Transient aeroelastic response for stabilized flight conditions at Mach = 1.00

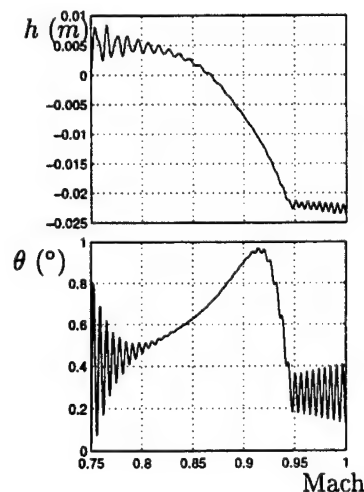


Fig. 6 Transient response during an accelerated flight: initial speed corresponds to Mach 0.75 and is increased by 0.05 Mach/second



speed corresponds to Mach number 0.84, and the initial excitation is effected by the same initial conditions as previously. We report in Fig. 7 the computed aeroelastic response. This response is characterized by larger amplitudes of vibration between Mach 0.85 and Mach 0.95, and confirms that flutter or limit cycle oscillations initiate around Mach 1.0.

Finally, we report in Fig. 8 the simulated aeroelastic response of the accelerated typical wing section after re-excitation at Mach 1.04.

#### 4.4 Parameter identification using the ERA: stabilized vs. accelerated flight scenarios

As stated in Section 3, the ERA assumes a constant sampling rate. Since our numerical simulations are not performed with a constant time-step  $\Delta t$ , we post-process our simulation results by a quadratic interpolation scheme in order to generate signals with

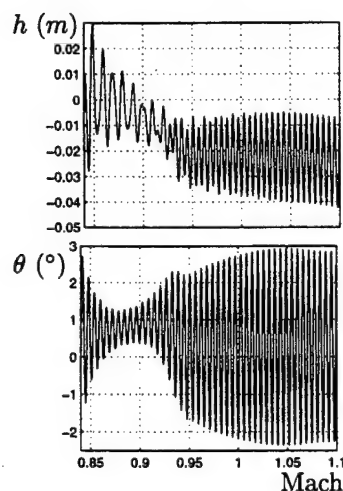


Fig. 7 Transient response during an accelerated flight: initial speed corresponds to Mach 0.84 and is increased by 0.05 Mach/second

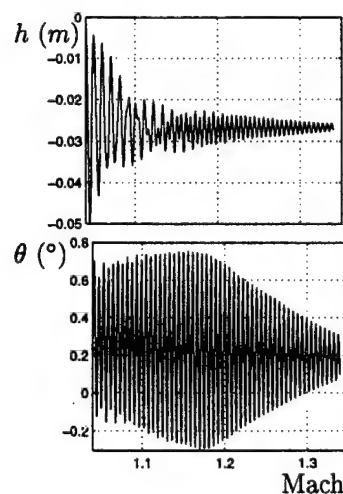


Fig. 8 Transient response during an accelerated: initial speed corresponds to Mach 1.04 and is increased by 0.05 Mach/second

a constant sampling rate.

The typical wing section described in this paper has 2 d.o.f. However, the *aeroelastic* typical wing section has more than 2 d.o.f., because of the surrounding fluid. For this reason, in all cases discussed in this section, we set the number of states for the synthesized system to  $n_x = 10$ , as if the system contained 5 d.o.f.

Our experience is that the ERA requires two cycles of the lowest mode contributing to the signal, and about 500 sampling points per cycle in order to identify accurately our system. Hence, in this work we set the parameters of the ERA as follows

$$\begin{aligned} 1000 &\leq N \leq 6000 \\ 500 &\leq q \leq 1000 \\ 500 &\leq d \leq 5000 \\ 2\frac{T_1}{N} &\leq \Delta t_S \leq 3\frac{T_1}{N} \\ n_x &= 10 \end{aligned}$$

where  $\Delta t_S$  is the sampling time, and  $T_1$  is the period of the lowest mode. We have verified *a posteriori* that the ERA configured with the above parameters produced excellent results for all applications discussed in this paper. Nevertheless, we note that higher values of the number of samples  $N$  and higher values of  $q$  improve the accuracy of the identification, but increase its cost.

As explained in Section 3, in order to extract the aeroelastic parameters of the typical wing section from the signals generated by the accelerated flight simulations, we propose to employ the ERA with windowing. The size of each time-window is  $N\Delta t_S$ . Given that the frequency of the first wet mode of the system can be expected to be close to that of the first dry mode of the system — that is, to 4.7 Hz — it follows that the size of each time-window varies between 0.4 second and 0.6 second. Hence, for an acceleration of 0.05 Mach/second, the maximum variation of the Mach number within a time-window is about 0.03 Mach. The significance of this variation depends on how fast the damping coefficient of the structure varies with the Mach number, which depends on the flow regime. Extensive experiments have revealed that when using the ERA with windowing, the identification results are to some extent insensitive to small variations in the size of the time-window and/or the values of  $n_x$ ,  $q$ , and  $d$ .

The frequencies and damping ratios identified by the FastERA using stabilized and accelerated flight simulation data are reported in Fig. 9. The following observations are noteworthy

- our typical wing section exhibits flutter for the second (torsional) mode in the transonic regime, for  $0.89 \leq M_\infty \leq 1.1$ .

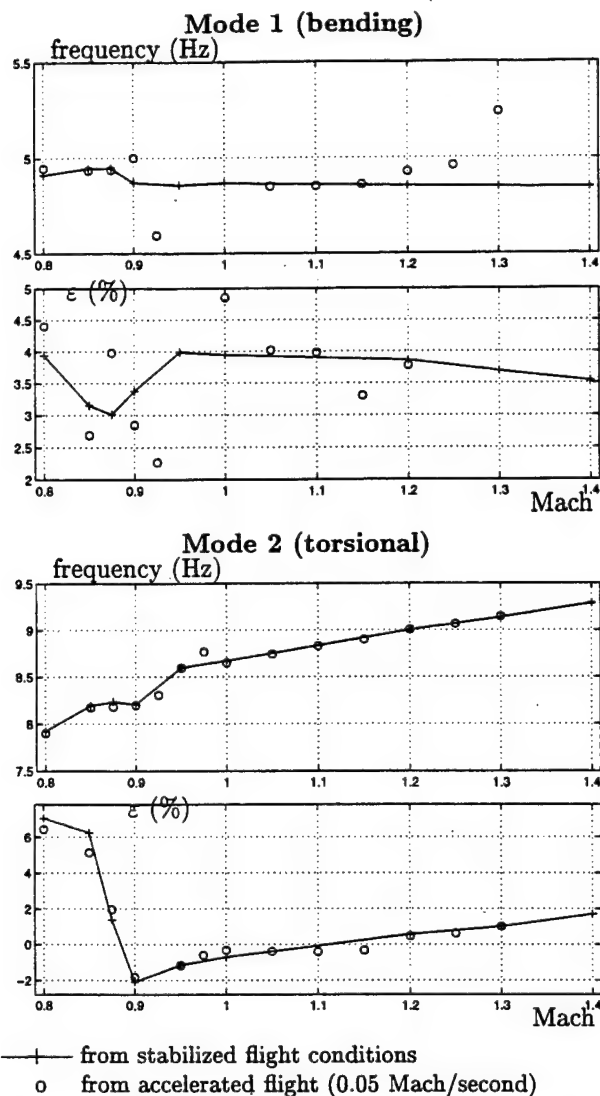


Fig. 9 Identified frequencies and damping ratios

- a sharp decrease of the damping ratio  $\varepsilon_2$  of the torsional mode occurs around Mach 0.9, and a slow increase of that damping ratio occurs above Mach 0.92. The same trend is also observed for the damping ratio  $\varepsilon_1$  of the first mode; however,  $\varepsilon_1$  remains positive.
- the frequency of the first mode appears to be almost independent of the Mach number. On the other hand, the frequency for the torsional mode, which is responsible here for flutter, slightly increases with the Mach number.
- occasionally, the frequencies and damping ratios identified for the first mode in simulated accelerated flight are reported to be different from those identified using stabilized flight simulated data. This is due to the fact that in our accelerated flight simulation, because the system is excited only at the beginning of the flight segment, after a certain amount of time, the contribution of the first mode to the signal can no longer be identi-

fied because it becomes significantly damped out. Re-exciting the system every second or so cures this problem.

- for the second mode, the frequencies and damping ratios identified for the stabilized and accelerated flight scenarios are in good agreement.

## 5 Validation

Here, we compare our simulated flight results to flight test data provided by the Edwards Air Force Base. The simulation results and test data are for the same stabilized flight conditions, but not the same F-16 configuration. The typical wing section designed in this paper is for a clean-wing configuration of the F-16. The flight test data provided by the Edwards Air Force Base is for a configuration of the F-16 that includes pylons and missiles. Nevertheless, Fig. 10 shows that our predicted wet frequencies are in good agreement with those measured in flight test. However, our predicted damping ratios do not agree well with the experimental data, even though the trend of their variation with the Mach number is similar to that of the flight test data. We can reasonably argue that a major cause of this discrepancy is the typical wing section model, which is supposed to be realistic only for fairly homogeneous wings with high aspect ratios and small angles of sweep. Other possible causes are the pylons, missiles, and viscous effects that are not accounted for in our flow computations. Perturbing the parameters of the typical wing section can improve the simulation results. For example, if the position of the elastic center of the typical wing section is shifted to 35% of the chord, our numerical simulations produce results that are in better agreement with the flight test data as demonstrated in Fig. 11.

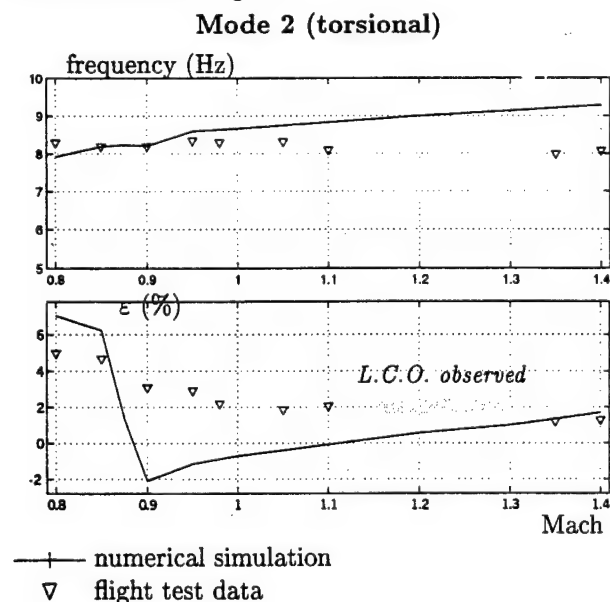


Fig. 10 Validation

## Mode 2 (torsional)

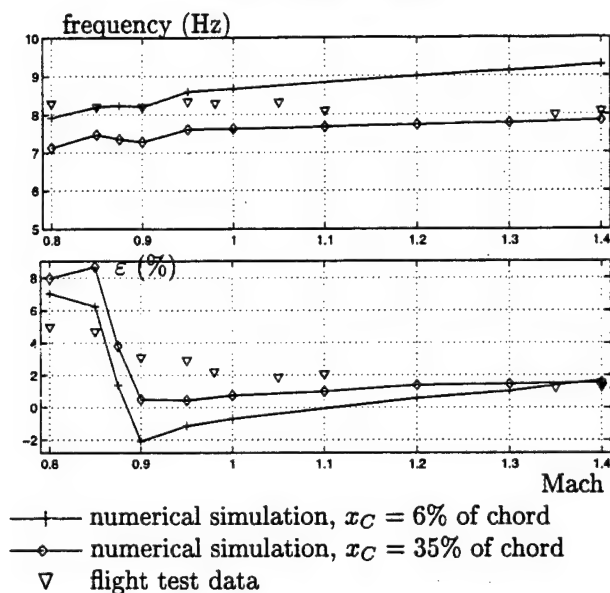


Fig. 11 Sensitivity of the aeroelastic parameters to the position of the elastic center

## 6 Conclusions

The wet frequencies and damping ratios of an aircraft are functions of the free-stream Mach number. Therefore, during an accelerated flight, these parameters become time-dependent. For this reason, theory suggests that standard signal processing techniques, which are limited to time-invariant systems, cannot be applied to the identification of an accelerated aeroelastic system. However, within a time-window of 0.2 second, and for a typical level flight acceleration of 1g or 0.03 Mach/second, the Mach number varies by 0.6% only. Hence, within a time-window of 0.2 second, the aeroelastic parameters of an aircraft can be assumed to remain constant. Such a time-window corresponds to 2 cycles of a mode at 10 Hz, a frequency that is relevant to the first bending and torsion modes of most aircraft. Therefore, any signal processing technique that can identify correctly a mode from 2 cycles of its response is a candidate technique for identifying the parameters of an accelerated aeroelastic system in a window-by-window approach. Furthermore, the analytical study of the typical wing section shows that realistic level flight accelerations do not affect the frequencies and damping ratios of an aeroelastic system. In other words, the aeroelastic parameters of an aircraft identified during an accelerated flight are the same as those identified in stabilized flight conditions. Hence, we conclude that there is a hope that flutter testing could be performed in accelerated flight, thereby reducing the cost and risk involved in determining the flutter envelopes of fighters. In practice, technical details such as re-excitation procedures, real-time identification, and flutter early alert systems must be addressed to enable such a technology.

## 7 Acknowledgements

The authors acknowledge the support by the Air Force Office of Scientific Research under Grant F49620-99-1-0037.

## References

- <sup>1</sup>R.L. Bisplinghoff and H. Ashley, *Principles of Aeroelasticity*, Dover Publication, New York, 1975.
- <sup>2</sup>J. Donea, *An Arbitrary Lagrangian-Eulerian Finite Element Method for Transient Fluid-Structure Interactions*, Comput. Meths. Appl. Mech. Engrg. 1982, 33: 689-723.
- <sup>3</sup>C. Farhat, M. Lesoinne and N. Maman, *Mixed Explicit/Implicit Time Integration of Coupled Aeroelastic Problems: Three-Field Formulation, Geometric Conservation and Distributed Solution*, Internat. J. Numer. Meths. Fluids 1995, 21: 807-835.
- <sup>4</sup>M. Lesoinne and C. Farhat, *Geometric Conservation Laws for Aeroelastic Computations Using Unstructured Dynamic Meshes*, AIAA Paper 95-1709, 12th AIAA Computational Fluid Dynamics Conference, San Diego, June 19-22, 1995.
- <sup>5</sup>M. Lesoinne and C. Farhat, *Geometric Conservation Laws for Flow Problems with Moving Boundaries and Deformable Meshes, and Their Impact on Aeroelastic Computations*, Comput. Meths. Appl. Mech. Engrg. 1996, 134:71-90.
- <sup>6</sup>L. Fezoui and B. Stoufflet, *A Class of Implicit Upwind Schemes for Euler Simulations with Unstructured Meshes*, J. Comp. Phys. 1989, 84:174-206.
- <sup>7</sup>C. Farhat, L. Fezoui, and S. Lanteri, *Two-Dimensional Viscous Flow Computations on the Connection Machine: Unstructured Meshes, Upwind Schemes, and Massively Parallel Computations*, Comput. Meths. Appl. Mech. Engrg. 1993, 102:61-88.
- <sup>8</sup>C. Farhat and S. Lanteri, *Simulation of Compressible Viscous Flows on a Variety of MPPs: Computational Algorithms for Unstructured Dynamic Meshes and Performance Results*, Comput. Meths. Appl. Mech. Engrg. 1994, 119:35-60.
- <sup>9</sup>B. NKonga and H. Guillard, *Godunov Type Method on Non-Structured Meshes for Three-Dimensional Moving Boundary Problems*, Comput. Meths. Appl. Mech. Engrg. 1994, 113:183-204.
- <sup>10</sup>B. Koobus and C. Farhat, *Second-Order Time-Accurate and Geometrically Conservative Implicit Schemes for Flow Computations on Unstructured Dynamic Meshes*, AIAA Paper 98-0113, 36th Aerospace Sciences Meeting and Exhibit, Reno, Nevada, January 12-15, 1998.
- <sup>11</sup>B. Koobus and C. Farhat, *Second-Order Time-Accurate and Geometrically Conservative Implicit Schemes for Flow Computations on Unstructured Dynamic Meshes*, Comput. Meths. Appl. Mech. Engrg. 1999, 170:103-130.
- <sup>12</sup>M. Lesoinne and C. Farhat, *A Higher-Order Subiteration Free Staggered Algorithm for Nonlinear Transient Aeroelastic Problems*, AIAA J. 1998, 36:1754-1756.
- <sup>13</sup>J.-N. Juang and R.S. Pappa, *An Eigensystem Realization Algorithm (ERA) for Modal Parameter Identification and Model Reduction*, J. of Guidance, Control, and Dynamics 1985, 8:620-627.
- <sup>14</sup>L.D. Peterson, *Efficient Computation of the Eigensystem Realization Algorithm*, J. Guidance, Control, and Dynamics 1995, 18:395-403.
- <sup>15</sup>L.D. Peterson, S.J. Bullock and S.X. Doebeling, *The Statistical Sensitivity of Experimental Modal Frequencies and Damping Ratios to Measurement Noise*, Internat. J. of Anal. Exp. Modal Anal. 1996, 11:63-75. AIAA, Aerospace Sciences Meeting and Exhibit, 37th, Reno, NV, Jan. 11-14, 1999.

# Application of a Three-Field Nonlinear Fluid-Structure Formulation to the Prediction of the Aeroelastic Parameters of an F-16 Fighter

Charbel Farhat\*, Philippe Geuzaine and Gregory Brown

Department of Aerospace Engineering Sciences

and Center for Aerospace Structures

University of Colorado at Boulder

Boulder, CO 80309-0429, U.S.A.

## Abstract

We overview a three-field formulation of coupled fluid-structure interaction problems where the flow is modeled by the arbitrary Lagrangian-Eulerian form of either the Euler or Navier-Stokes equations, the structure is represented by a detailed finite element model, and the fluid grid is unstructured, dynamic, and constructed by a robust structure analogy method. We discuss the latest advances in the computational algorithms associated with this approach for modeling aeroelastic problems. We apply the three-field nonlinear computational framework to the prediction of the aeroelastic frequencies and damping coefficients of an F-16 configuration in various subsonic, transonic, and supersonic regimes. We consider for this purpose both the popular two-dimensional typical wing section model and a detailed three-dimensional finite element model of the structure, and compare in both cases the obtained numerical results with flight test data. We comment on the advantages and shortfalls of both approaches, and on the feasibility as well as the merit of the three-field formulation of nonlinear aeroelasticity for the extraction of flutter envelopes.

**Key words.** Aeroelasticity, F-16 fighter, fluid-structure interaction, flutter, CFD on moving grids.

---

\*Corresponding Author

# 1 Introduction

If an elastic aircraft immersed in an unsteady flow undergoes a damped harmonic motion characterized by *small displacement amplitudes*, a *wet* (or aeroelastic) circular frequency  $\bar{\omega}$ , and a *wet* positive or negative damping coefficient  $\bar{\alpha}$ , and if the airflow surrounding it can be accurately predicted by an *inviscid linearized theory*, then aeroelastic stability problems such as flutter can be cast into an eigenvalue problem of the form [1]

$$\mathbf{Z}_m(\bar{k}) \mathbf{y}_m = \left( \frac{1}{\bar{\omega}^2} - i \frac{2\bar{\alpha}}{\bar{\omega}^2} \right) \mathbf{y}_m \quad (1)$$

where  $\mathbf{Z}_m \in \mathbb{R}^{m \times m}$  is given by

$$\mathbf{Z}_m(\bar{k}) = \Omega_m^2{}^{-1} \left( \mathbf{I}_m - \frac{1}{2} \frac{\rho_\infty}{\bar{k}^2} \mathbf{A}_m(\bar{k}) \right) \quad (2)$$

and  $i$  is the complex imaginary number satisfying  $i^2 = -1$ . Here,  $M_\infty$ ,  $V_\infty$ , and  $\rho_\infty$  denote the free-stream Mach number, velocity, and density of the flow.  $\bar{k} = \bar{\omega}/V_\infty$  is the reduced aeroelastic circular frequency associated with  $\bar{\omega}$ .  $\Omega_m^2$  is a diagonal matrix storing the squares of the first  $m$  fundamental circular frequencies  $\omega_i$  of the dry aircraft, and  $\mathbf{I}_m$  is the identity matrix of dimension  $m$ . Typically, the aircraft structure is represented by its first 20 to 40 dry (or ground) modes, and therefore  $20 \leq m \leq 40$ .  $\mathbf{A}_m$  denotes the projection of a linear aerodynamic operator  $\mathbf{A}$  onto the  $m$ -dimensional modal basis associated with  $\Omega_m^2$ , and  $\mathbf{y}_m$  denotes the projection of the amplitude of the aircraft's motion onto that basis.

A critical value of  $\bar{k}$ ,  $\bar{k}^{cr}$ , is that for which  $\mathbf{Z}_m$  has a real eigenvalue equal to  $1/\bar{\omega}_i^{cr^2}$  ( $1 \leq i \leq m$ ). From Eq. (1), it follows that for  $\bar{k} = \bar{k}^{cr}$ , the damping coefficient  $\bar{\alpha}_i^{cr}$  of the  $i$ -th aeroelastic mode vanishes. Hence, given a free-stream Mach number and a free-stream density, the critical value of the reduced frequency, if it exists, can be found by sweeping on  $\bar{k}$  and solving the eigenvalue problem (1) until a real eigenvalue is found. In that event, the flutter mode of the aircraft is the mode  $i$  for which  $\bar{\alpha}_i^{cr} = 0$ , the flutter speed of the aircraft is  $V_\infty^{cr} = \bar{\omega}_i^{cr}/\bar{k}^{cr}$ , and the flutter dynamic pressure is  $\lambda^{cr} = \rho_\infty V_\infty^{cr^2}/2$ . Such a procedure for extracting the flutter speed of an aircraft is known as the "k" method [2]. It is accurate when the assumptions stated above hold, and when the structure is less than 10% damped. When the structure has a higher percentage of damping, an improved version of this procedure known as the "p-k" method [3] is preferable for finding the flutter dynamic pressure. Assuming that the positive or negative  $\bar{\alpha}_i$  coefficients are small, the variations of the aeroelastic frequencies and damping coefficients with the Mach number,  $\bar{\omega}_i(M_\infty)$  and  $\bar{\alpha}_i(M_\infty)$ ,  $1 \leq i \leq m$ , can also be predicted by sweeping on  $M_\infty$  and solving the eigenvalue problem (1).

The "k", "p-k" and other similar procedures for flutter analysis are based on the *linear* theory of aeroelasticity whose assumptions have been stated at the beginning of this introduction. They are fast and memory lean. For this



reason, they are also popular in the aerospace industry. In the subsonic regime, most if not all of these procedures rely today on the doublet-lattice method [4] for computing the linear aerodynamic operator  $A$ . It is interesting to note that this method, which was developed over thirty years ago, is still today the most used method for predicting subsonic unsteady flows in production environments, particularly for load and flutter analyses. In the supersonic regime, various methods related to the piston theory [5] are used for constructing  $A$ .

High performance military aircraft are usually flutter critical in the transonic speed range at high dynamic pressure. Unfortunately, in that regime, the mixed subsonic-supersonic flow patterns and shock waves are such that the linear flow theory in general — and therefore the doublet-lattice method in particular — are not reliable for predicting the unsteady aerodynamic forces acting on an aircraft. As a result, flutter testing of a scaled model in a transonic wind tunnel is always used to generate corrections to flutter speeds computed by linear methods. However, the design, construction and testing of a wind tunnel flutter model, and the analysis of the resulting data, require over a year's time. For this reason, leading authorities in this field have recently suggested [6] that *"The results of a finite number of [nonlinear] CFD [computational fluid dynamics] solutions could be used as a replacement for wind tunnel testing, assuming a validated code was available."* Coincidentally, this paper addresses this very same issue in the context of an F-16 Block 40 fighter.

More specifically, our objectives here are to overview a three-field formulation of fluid-structure interaction problems for nonlinear computational aeroelasticity, assess the latest advances in the corresponding CFD and CSM (computational structural mechanics) algorithms, briefly describe a high-performance simulation software developed at the University of Colorado based on these ideas, report on its validation with flight test data for an F-16 Block 40 configuration, and discuss the feasibility as well as the merit of this computational strategy for extracting accurately the flutter envelopes of high performance civilian and military aircraft. To this effect, we organize the remainder of this paper as follows.

In Section 2, we overview a three-field formulation of coupled fluid-structure interaction problems that is flexible enough to accommodate all types of nonlinearities. In Section 3, we identify the main computational issues associated with this formulation. For some of these issues, we take a new look at the latest developments and achievements, and highlight their impact on the overall performance of the solution of nonlinear aeroelastic problems. In Section 4, we briefly describe the CFD/CSM based simulation software developed at the University of Colorado for solving general aeroelastic problems. This software is based on the three-field formulation and incorporates all the advances in the computational methods described in this paper. In Section 5, we apply this simulation software to the prediction of the aeroelastic frequencies and damping coefficients of an F-16 Block 40 configuration in various subsonic, transonic, and supersonic regimes. For this purpose, we represent first this fighter by its typical wing section. Then, we consider a three-dimensional detailed finite element (FE) model of its structure. In both cases, we comment on the obtained

numerical results and compare them to the measured flight test data. Finally in Section 6, we conclude this paper by a discussion of the feasibility and merit of our CFD/CSM based methodology for the flutter analysis of high performance aircraft in the transonic and other regimes.

## 2 Three-field formulation of nonlinear aeroelastic problems

First, we overview a three-field formulation of coupled fluid-structure interaction problems that was first introduced in [7]. This formulation is quite general. It can address many aeroelastic problems besides flutter, including the prediction of steady and unsteady loads as well as control surface effects in level flight as well as during maneuvering, aeroelastic tailoring, and performance analysis. In this formulation, the structure is no longer restricted to a harmonic motion with small displacement amplitudes, and is not necessarily represented by a truncated basis of its normal modes. In principle, there is also no reason to confine its constitutive modeling to that of an elastic material. However, while aircraft structures can undergo large displacements and rotations, they seldom experience large strains. Therefore in many applications, the nonlinear modeling of the structural behavior can be limited to the proper accounting of nonlinear geometric and free play effects. More importantly, the aerodynamic forces acting on the structure are no longer predicted in this formulation by the use of a linear aerodynamic operator, because of the limitations associated with such an approach, particularly in the transonic regime. Rather, these unsteady forces are determined from the solution of the compressible Euler equations when viscous effects can be neglected, and the solution of the compressible Navier-Stokes equations augmented by a large eddy simulation or turbulence model otherwise. Furthermore, no restriction is imposed on the nature of the fluid-structure coupling, which is numerically modeled by suitable fluid-structure interface boundary (or transmission) conditions. One difficulty in handling numerically the fluid-structure coupling stems from the fact that the structural equations are usually formulated with material (Lagrangian) coordinates, while the fluid equations are typically written using spatial (Eulerian) coordinates. Therefore, a straightforward approach to the solution of the coupled fluid-structure dynamic equations requires moving at each time-step at least the portions of the fluid grid that are close to the moving and flexing aircraft. This can be appropriate for small displacements of the structure but may lead to severe grid distortions when it undergoes large motion. Different approaches have emerged as an alternative to partial regridding in transient aeroelastic computations, among which stand out the arbitrary Lagrangian-Eulerian (ALE) formulation [8] and the closely related method of dynamic meshes [9]. These approaches treat a computational aeroelasticity problem as a two-field coupled problem. However, a moving mesh (Fig. 1) can also be viewed as a pseudo-structural (or fictitious structural) system with its own behavior [7], and therefore, the coupled transient aeroelastic

problem can be formulated as a *three-* rather than two-field problem: the fluid, the structure, and the dynamic fluid mesh. This three-field formulation has shed new light on the mathematical understanding of the numerical behavior of various algorithms applied to the solution of the coupled fluid-structure problem, and has enabled the development of faster solution algorithms [10–14].

Clearly, the simultaneous solution of the governing nonlinear fluid, fluid mesh, and structure equations of motion is computationally intensive, and raises some concerns about the feasibility and practical usefulness of this approach in production environments. An important objective of this paper is to show that because of significant advances in computational methods and the advent of parallel processing, the three-field and CFD/CSM based solution of aeroelastic problems is now sufficiently mature and fast to be considered at least as a reliable simulation environment, if not to be adopted as a design tool, for addressing the critical flight conditions of a high performance aircraft.

## 2.1 Governing multidisciplinary equations

A fluid-structure interaction problem can be described by the following coupled partial differential equations

$$\frac{\partial(Jw)}{\partial t}|_{\xi} + J\nabla_x \cdot (F(w) - \frac{\partial x}{\partial t} w) = J\nabla_x \cdot R(w) \quad (3a)$$

$$\rho_S \frac{\partial^2 u_S}{\partial t^2} - \text{div}(\sigma_S(\epsilon_S(u_S), \frac{\partial \epsilon_S}{\partial t}(u_S))) = b \quad (3b)$$

$$\bar{\rho} \frac{\partial^2 x}{\partial t^2} - \text{div}(\bar{\sigma}(\bar{\epsilon}(x))) = 0 \quad (3c)$$

Equation (3a) is the ALE conservative form of the Navier-Stokes equations. Here,  $t$  denotes the time,  $x(t)$  denotes the time-dependent position or displacement of a fluid grid point (depending on the context of the sentence and the equation),  $\xi$  its position in a reference configuration,  $J = \det(dx/d\xi)$ ,  $w$  is the fluid state vector using the conservative variables, and  $F$  and  $R$  denote respectively the convective and diffusive ALE fluxes. Equation (3b) is the elastodynamic equation where  $u_S$  denotes the displacement field of the structure and  $\rho_S$  its density,  $\sigma_S$  and  $\epsilon_S$  denote respectively the stress and strain tensors, and  $b$  represents the body forces acting on the given structure. Equation (3c) governs the dynamics of the moving fluid grid. It is similar to the elastodynamic equation because the dynamic mesh is viewed here as a pseudo-structural system. A tilde notation is used to designate the fictitious mechanical quantities [1]. For the sake of notational simplicity, the various Dirichlet and Neumann boundary conditions intrinsic to each of the fluid and structure problems are omitted.

Equation (3a) and equation (3c) are directly coupled. If  $u_F$  denotes the ALE displacement field of the fluid and  $p$  its pressure field,  $\sigma_S$  and  $\sigma_F$  the structure stress tensor and the fluid viscous stress tensor,  $\Gamma$  the fluid-structure interface boundary (wet boundary of the structure), and  $n$  the normal at a point to  $\Gamma$ , the fluid and structure equations are coupled by the interface boundary — or

transmission — conditions

$$\sigma_S \cdot n = -pn + \sigma_F \cdot n \quad \text{on } \Gamma \quad (4a)$$

$$\frac{\partial u_S}{\partial t} = \frac{\partial u_F}{\partial t} \quad \text{on } \Gamma \quad (4b)$$

The first of these two transmission conditions states that the tractions on the wet surface of the structure are in equilibrium with those on the fluid side of  $\Gamma$ . The second of Eqs. (4) expresses the compatibility between the velocity fields of the structure and the fluid at the fluid-structure interface. For inviscid flows, this second equation is replaced by the slip wall boundary condition

$$\frac{\partial u_F}{\partial t} \cdot n = \frac{\partial u_S}{\partial t} \cdot n \quad \text{on } \Gamma \quad (5)$$

The equations governing the structure and dynamic mesh motions are coupled by the continuity conditions

$$x = u_S \quad \text{on } \Gamma \quad (6a)$$

$$\frac{\partial x}{\partial t} = \frac{\partial u_S}{\partial t} \quad \text{on } \Gamma \quad (6b)$$

## 2.2 Semi-discretization of the governing equations

The spatial approximation of the ALE conservative form of the Navier-Stokes equations by FE or finite volume (FV) schemes leads to semi-discrete equations that can be written as

$$(\dot{\mathbf{V}}(\mathbf{x})\mathbf{w}) + \mathbf{F}(\mathbf{w}, \mathbf{x}, \dot{\mathbf{x}}) = \mathbf{R}(\mathbf{w}, \mathbf{x}) \quad (7)$$

where a bold font designates the discrete counterpart of a field variable, and a dot a time derivative. In the case of a FV semi-discretization,  $\mathbf{V}$  is the matrix of the cell volumes and  $\mathbf{F}$  and  $\mathbf{R}$  are respectively the numerical convective and diffusive fluxes approximating the integral of the physical flux function over the cell interfaces.

The semi-discretization by FE of the structural equations of dynamic equilibrium leads to<sup>1</sup>

$$\mathbf{M}\ddot{\mathbf{u}}_S + \mathbf{f}_S^{int}(\mathbf{u}_S, \dot{\mathbf{u}}_S) = \mathbf{f}_S^{ae}(\mathbf{u}_S, \mathbf{w}) + \mathbf{f}_S^{ext} \quad (8)$$

where  $\mathbf{M}$  is the FE lumped mass matrix,  $\mathbf{u}_S$  the generalized displacement vector,  $\mathbf{f}_S^{int}$  the vector of internal forces,  $\mathbf{f}_S^{ae}$  the vector of aerodynamic forces applied on the wet surface of the structure, and  $\mathbf{f}_S^{ext}$  the vector of other external forces acting on the structure. If for the problem of interest the structure remains linear, Eq. (8) simplifies to

$$\mathbf{M}\ddot{\mathbf{u}}_S + \mathbf{C}\dot{\mathbf{u}}_S + \mathbf{K}\mathbf{u}_S = \mathbf{f}_S^{ae}(\mathbf{u}_S, \mathbf{w}) + \mathbf{f}_S^{ext} \quad (9)$$

<sup>1</sup>This specific expression assumes that the rotational inertia forces are negligible.

where  $C$  and  $K$  denote the FE damping and stiffness matrices.

Let the subscript  $i$  designate the grid points located in the interior of a computational domain, and the subscript  $b$  designate those grid points located at the fluid-structure interface  $\Gamma$ . If the dynamic mesh is assimilated with a *quasi-static* pseudo-structural system, the semi-discrete equation governing the evolution of the dynamic mesh can be written as

$$\widetilde{K}_{ii}x_i = -\widetilde{K}_{ib}x_b \quad x_b = Uu_{S_b} \quad (10)$$

where  $\widetilde{K}$  is the fictitious time-dependent stiffness matrix resulting from the FE semi-discretization of Eq. (3c) [1], and  $U$  is a transfer matrix. If the fluid and structure meshes have compatible interfaces,  $U = I$ . Otherwise,  $U$  is given by the FE discretization of the second of the interface conditions (4).

### 3 Computational issues and advances

In the linear theory of aeroelasticity, the air surrounding a flying aircraft can be interpreted as an "algebraic" damper whose sign depends on the flight conditions. When positive, it attenuates any aircraft vibration excited by some initial disturbance. When zero, it only entertains it, and when negative, it amplifies that vibration. In other words, depending on the flight conditions and particularly the Mach number, the air surrounding a vibrating aircraft can either extract energy from it, or act as a neutral agent towards it, or feed it energy and cause it to flutter. This energy interpretation of the flutter mechanism underscores the importance of *conserving* as much as possible the energy transferred between the fluid and structure subsystems when discretizing the transmission conditions (4) and solving the coupled system of equations (7, 8, 10). Indeed, the extraction (transmission) from (to) the structure across the fluid-structure interface  $\Gamma$  of any significant amount of spurious numerical energy can artificially stabilize (destabilize) an otherwise unstable (stable) aeroelastic system. Since the three-field aeroelastic problem (7, 8, 10) is formulated in the time domain, extracting the wet frequencies and damping coefficients of the underlying structure for flutter analysis requires post-processing the numerical output — for example, the displacement field  $\bar{u}_s(t)$  — by a parameter identification algorithm. Computational efficiency suggests using for that purpose an identification algorithm that requires as few cycles as possible of the predicted structural response. This in turn underscores the importance of producing a sufficiently accurate short window of the time-response, and therefore time-integrating the *coupled* fluid-structure and not *individual* fluid and structure equations of motion (7, 8) with a second-order time-accurate scheme. Usually, the aeroelastic response of the structure is dominated by its low modes. For this reason, computational speed — which is essential for production environments — favors implicit schemes and large computational steps, which underscores the importance of paying special attention to the numerical stability properties of the scheme designed for time-integrating the coupled fluid-structure equations of



motion. Next, we review some recent achievements in these areas. Because of space limitation, we focus on discussing results, and refer the reader to the appropriate literature for details.

### 3.1 CFD on moving unstructured grids

The governing fluid equation (7) differs from the standard FE or FV semi-discretization of the Navier-Stokes equations in that it is formulated on a moving rather than a fixed grid. Therefore, the time-discretization of this equation, which incurs the approximation of the integrals  $\int_{t^n}^{t^{n+1}} \mathbf{F}(\mathbf{w}, \mathbf{x}, \dot{\mathbf{x}}) dt$  and  $\int_{t^n}^{t^{n+1}} \mathbf{R}(\mathbf{w}, \mathbf{x}) dt$ , raises the question of where to evaluate the convective and diffusive fluxes when the grid moves from its position  $\mathbf{x}^n$  at time  $t^n$  to a position  $\mathbf{x}^{n+1}$  at time  $t^{n+1}$ . A straightforward answer to this question is to evaluate these fluxes on the mesh configuration  $\mathbf{x}^n$  when the chosen time-integrator is explicit, and  $\mathbf{x}^{n+1}$  when the time-integrator is implicit. For small time-steps  $\Delta t^n = t^{n+1} - t^n$ , it may not matter where the fluxes are evaluated because in that case the difference between the mesh configurations  $\mathbf{x}^n$  and  $\mathbf{x}^{n+1}$  may be insignificant. However, for the large time-steps dictated by computational efficiency, the method of evaluation of the integrals  $\int_{t^n}^{t^{n+1}} \mathbf{F}(\mathbf{w}, \mathbf{x}, \dot{\mathbf{x}}) dt$  and  $\int_{t^n}^{t^{n+1}} \mathbf{R}(\mathbf{w}, \mathbf{x}) dt$  can have a dramatic effect on the performance of the time-integration of the governing fluid equation (7). To address this issue, it was proposed in [10–13] to first select a time-integrator that performs well on fixed grids, and then extend it to moving grids by evaluating a moving flux as the time-average of a certain number of fluxes computed on a suite of carefully chosen mesh configurations. For example, the classical three-point backward difference scheme fits well the selection criteria stated in the introduction of this section: it is implicit, second-order time-accurate on fixed grids, and unconditionally stable for the usual test problem on fixed grids. Its extension to moving grids as proposed in [10–13] can therefore be written as follows

$$\begin{aligned} \alpha_{n+1} \mathbf{V}^{n+1} \mathbf{w}^{n+1} + \alpha_n \mathbf{V}^n \mathbf{w}^n + \alpha_{n-1} \mathbf{V}^{n-1} \mathbf{w}^{n-1} \\ + \Delta t^n \sum_{s=1}^{n_s^c} c_s^c \mathbf{F}(\mathbf{w}^{n+1}, \mathbf{x}_s^c, \dot{\mathbf{x}}_s^c) - \Delta t^n \sum_{s=1}^{n_s^d} c_s^d \mathbf{R}(\mathbf{w}^{n+1}, \mathbf{x}_s^d) = 0 \quad (11) \end{aligned}$$

where

$$\alpha_{n+1} = \frac{1+2\tau}{1+\tau}, \quad \alpha_n = -1-\tau, \quad \alpha_{n-1} = \frac{\tau^2}{1+\tau}, \quad \tau = \frac{\Delta t^n}{\Delta t^{n-1}}$$

and  $\mathbf{V}^n = \mathbf{V}(\mathbf{x}^n)$ .  $n_s^c$  and  $n_s^d$  are two small integers, while  $c_s^c$  and  $c_s^d$  are real coefficients (averaging weights) that satisfy  $\sum_{s=1}^{n_s^c} c_s^c = 1$  and  $\sum_{s=1}^{n_s^d} c_s^d = 1$ .  $\mathbf{x}_s^c$ ,  $\mathbf{x}_s^d$ , and  $\dot{\mathbf{x}}_s^c$  are linear combinations of the mesh configurations  $\{\mathbf{x}^{n-l}, \dots, \mathbf{x}^n, \dots, \mathbf{x}^{n+m}\}$  and velocities  $\{\dot{\mathbf{x}}^{n-j}, \dots, \dot{\mathbf{x}}^n, \dots, \dot{\mathbf{x}}^{n+q}\}$  for some given integers  $l$ ,  $m$ ,  $j$ , and  $q$ . Note

that Eq. (11) anticipates two different time-averaging procedures for the moving convective and viscous fluxes.

The computational complexity of the scheme (11) can be reduced by averaging the mesh configurations themselves instead of the fluxes associated with them, which leads to

$$\begin{aligned} & \alpha_{n+1} V^{n+1} w^{n+1} + \alpha_n V^n w^n + \alpha_{n-1} V^{n-1} w^{n-1} \\ & + \Delta t^n F(w^{n+1}, \sum_{s=1}^{n_s^c} c_s^c x_s^c, \sum_{s=1}^{n_s^c} c_s^c \dot{x}_s^c) - \Delta t^n R(w^{n+1}, \sum_{s=1}^{n_s^d} c_s^d x_s^d) = 0 \quad (12) \end{aligned}$$

This alternative approach was proposed and discussed in [13] in the context of the FV semi-discretization of the governing flow equations. It requires the computation of a single convective flux and a single diffusive flux per time-step, whereas the approach summarized in Eq. (11) requires the computation at each time-step of  $n_s^c$  convective and  $n_s^d$  diffusive fluxes. In the remainder of this paper, we adopt the form (12) of the extension to moving grids of the three-point backward difference scheme. However, most of the results we present for that form also hold for the version (11) of that extension.

Whether scheme (11) or scheme (12) is chosen for extending the three-point backward difference scheme to moving grids, it remains to determine  $n_s^c$  and  $n_s^d$ , the averaging coefficients  $c_s^c$  and  $c_s^d$ , the mesh configurations  $x_s^c$ , and  $x_s^d$ , and the mesh velocities  $\dot{x}_s^c$ . To this effect, two approaches can be adopted. The first one consists in choosing these parameters so that the resulting time-integrator satisfies its corresponding discrete geometric conservation law (DGCL) [15, 16]. The second approach consists in selecting these parameters so that the resulting time-integrator remains second-order time-accurate on moving grids.

The so-called DGCL is a law which states that the computation of the geometric parameters associated with a moving grid should be performed in such a way that, independently of the mesh motion, the numerical scheme constructed for time-integrating the flow equations on a moving grid preserves the state of a uniform flow. The idea of computing the discrete mesh velocities and other geometric parameters as to preserve a certain physical quantity goes back to the early days of CFD. The terminology “geometric conservation law” was coined in 1979 by Thomas and Lombard [17] who derived this concept from the law of mass conservation in a spatial region bounded by a moving surface, and applied it to construct an improved finite difference method for flow computations on moving grids. This concept was subsequently extended to characterize geometrically conservative schemes as algorithms that preserve the entire state of a uniform flow. First-order time-accurate and geometrically conservative ALE FV schemes were presented and discussed in [11, 12, 18]. First-order time-accurate and geometrically conservative ALE FE schemes were presented in [11, 12]. DGCLs for second-order time-accurate ALE FV schemes have also been developed and discussed in [13]. For example, parameterizing the sought-after mesh configuration

$\mathbf{x}_s^c$  and its corresponding velocity field as suggested in [13]

$$\mathbf{x}_s^c = \eta_s^{n+1} \mathbf{x}^{n+1} + \eta_s^n \mathbf{x}^n + (1 - \eta_s^{n+1} - \eta_s^n) \mathbf{x}^{n-1} \quad (13a)$$

$$\dot{\mathbf{x}}_s^c = \theta_s^{n+1} \mathbf{x}^{n+1} + \theta_s^n \mathbf{x}^n - (\theta_s^{n+1} + \theta_s^n) \mathbf{x}^{n-1} \quad (13b)$$

and requiring that the scheme (12) satisfies its DGCL leads to a nonlinear system of equations in the unknowns  $n_s^c$ ,  $c_s^c$ ,  $\{\eta_s^{n+p}\}_{p=0}^{p=1}$ , and  $\{\theta_s^{n+p}\}_{p=0}^{p=1}$ . In the case of three dimensions and a FV semi-discretization method, one of the many possible solutions of that nonlinear system of equations leads to (see [13])

$$\begin{cases} n_s^c = 4; & c_1^c = c_2^c = \frac{\alpha_{n+1}}{2}; & c_3^c = c_4^c = -\frac{\alpha_{n-1}}{2\tau} \\ \mathbf{x}_1^c = \frac{1}{2}(1 - \frac{1}{\sqrt{3}})\mathbf{x}^{n+1} + \frac{1}{2}(1 + \frac{1}{\sqrt{3}})\mathbf{x}^n \\ \mathbf{x}_2^c = \frac{1}{2}(1 + \frac{1}{\sqrt{3}})\mathbf{x}^{n+1} + \frac{1}{2}(1 - \frac{1}{\sqrt{3}})\mathbf{x}^n \\ \mathbf{x}_3^c = \frac{1}{2}(1 - \frac{1}{\sqrt{3}})\mathbf{x}^n + \frac{1}{2}(1 + \frac{1}{\sqrt{3}})\mathbf{x}^{n-1} \\ \mathbf{x}_4^c = \frac{1}{2}(1 + \frac{1}{\sqrt{3}})\mathbf{x}^n + \frac{1}{2}(1 - \frac{1}{\sqrt{3}})\mathbf{x}^{n-1} \\ \dot{\mathbf{x}}_1^c = \dot{\mathbf{x}}_2^c = \frac{\mathbf{x}^{n+1} - \mathbf{x}^n}{\Delta t^n} \\ \dot{\mathbf{x}}_3^c = \dot{\mathbf{x}}_4^c = \frac{\mathbf{x}^n - \mathbf{x}^{n-1}}{\Delta t^{n-1}} \end{cases} \quad (14)$$

This completes the description of one instance of the scheme (12) that is based on a four-point discretization of the moving convective fluxes. Enforcing a DGCL cannot determine the coefficients  $c_s^d$  and mesh configurations  $\mathbf{x}_s^d$ , because the moving viscous fluxes vanish for a uniform flow. To determine these parameters, one can adopt the second approach mentioned above and described next.

Alternatively, the parameterization (13) and a similar parameterization of the sought-after mesh configuration  $\mathbf{x}_s^d$  can be substituted into the scheme (12). Next, the local truncation error of the resulting time-integration algorithm can be computed as usual by applying Taylor's expansion around the variables at  $t^n$ . Finally, the unknowns  $c_s^c$ ,  $c_s^d$ , and the parameters governing the mesh configurations  $\mathbf{x}_s^c$ ,  $\dot{\mathbf{x}}_s^c$  and  $\mathbf{x}_s^d$  can be determined by requiring that the zero-, first-, and second-order terms of the local truncation error vanish. It turns out that this second approach for determining  $c_s^c$ ,  $c_s^d$ ,  $\mathbf{x}_s^c$ ,  $\dot{\mathbf{x}}_s^c$ , and  $\mathbf{x}_s^d$  works equally well when  $n_s^c$  is set à priori to  $n_s^c = 4$ ,  $n_s^d$  and  $c_s^d$  are set à priori to  $n_s^d = 1$  and  $c_1^d = 1$ , and  $\mathbf{x}_s^d$  is parameterized differently than  $\mathbf{x}_s^c$  using the simpler linear map

$$\mathbf{x}_s^d = \zeta_s^{n+1} \mathbf{x}^{n+1} + (1 - \zeta_s^{n+1}) \mathbf{x}^n \quad (15)$$

which was first proposed in [22]. In that case, requiring that the scheme (12)

be second-order time-accurate on moving grids leads to

$$\sum_{s=1}^4 c_s^c = 1 \quad (16a)$$

$$\sum_{s=1}^4 c_s^c (\theta_s^{n+1} + \frac{\theta_s^{n+1} + \theta_s^n}{\tau}) = \frac{1}{\Delta t^n} \quad (16b)$$

$$\sum_{s=1}^4 c_s^c (\eta_s^{n+1} - \frac{1 - \eta_s^{n+1} - \eta_s^n}{\tau}) = 1 \quad (16c)$$

$$\sum_{s=1}^4 c_s^c (\theta_s^{n+1} - \frac{\theta_s^{n+1} + \theta_s^n}{\tau^2}) = \frac{2}{\Delta t^n} \quad (16d)$$

$$\zeta_s^{n+1} = 1 \quad (16e)$$

Again, the system of equations (16) admits multiple solutions, among which we note two solutions corresponding to the following averaging coefficients and mesh configurations

$$\begin{cases} n_s^c = 4; & c_1^c = 1; & c_2^c = c_3^c = c_4^c = 0 \\ x_1^c = x^{n+1} \\ \dot{x}_1^c = \frac{\alpha_{n+1}x^{n+1} + \alpha_n x^n + \alpha_{n-1}x^{n-1}}{\Delta t^n} \\ n_s^d = 1; & c_1^d = 1 \\ x_1^d = x^{n+1} \end{cases} \quad (17)$$

and

$$\begin{cases} n_s^c = 4; & c_1^c = c_2^c = \frac{\alpha_{n+1}}{2}; & c_3^c = c_4^c = -\frac{\alpha_{n-1}}{2\tau} \\ x_1^c = \frac{1}{2}(1 - \frac{1}{\sqrt{3}})x^{n+1} + \frac{1}{2}(1 + \frac{1}{\sqrt{3}})x^n \\ x_2^c = \frac{1}{2}(1 + \frac{1}{\sqrt{3}})x^{n+1} + \frac{1}{2}(1 - \frac{1}{\sqrt{3}})x^n \\ x_3^c = \frac{1}{2}(1 - \frac{1}{\sqrt{3}})x^n + \frac{1}{2}(1 + \frac{1}{\sqrt{3}})x^{n-1} \\ x_4^c = \frac{1}{2}(1 + \frac{1}{\sqrt{3}})x^n + \frac{1}{2}(1 - \frac{1}{\sqrt{3}})x^{n-1} \\ \dot{x}_1^c = \dot{x}_2^c = \frac{x^{n+1} - x^n}{\Delta t^n} \\ \dot{x}_3^c = \dot{x}_4^c = \frac{x^n - x^{n-1}}{\Delta t^{n-1}} \\ n_s^d = 1; & c_1^d = 1 \\ x_1^d = x^{n+1} \end{cases} \quad (18)$$

It follows that at least two different instances of the parameterized time-integrator (12) achieve second-order accuracy on moving grids. The first one is based on the one-point rule described by Eqs. (17). This algorithm does not however satisfy its DGCL (for a proof, the reader can simply verify that Eqs. (17) do not satisfy the DGCL requirements of the time-integrator (12) which are listed in [13]). The second instance of the parameterized time-integrator (12) is based

on the four-point rule described by Eqs. (18), which is identical to that described by Eqs. (14); hence, this second instance of scheme (12) satisfies its DGCL. Therefore, using what we have referred to as the second approach for extending the three-point backward difference scheme to moving grids, one can construct different time-integrators for the governing semi-discrete fluid equations (7) that are all second-order time-accurate, but which do not necessarily satisfy their DGCL. This is consistent with the following theoretical result established by Guillard and Farhat [15, 16]: “for a given scheme that is  $p$ -order time-accurate on a fixed mesh, satisfying the corresponding  $p$ -discrete geometric conservation law is [only] a sufficient condition for this scheme to be at least first-order time-accurate on a moving mesh”. Therefore, the question becomes whether there is any particular reason to discriminate between those second-order extensions to moving grids of the three-point backward difference scheme that satisfy their DGCLs, and those that do not satisfy it?

In [10, 12], it was shown numerically that for typical aeroelastic computations, violating the DGCL can introduce a parasitic weak instability in the lift response, and can lead to the prediction of an erroneous flutter speed. Motivated by these observations, Formaggia and Nobile have investigated the solution of *linear* advection-diffusion problems on moving grids by ALE FE methods [20]. They have shown that for these linear problems, satisfying the corresponding first-order discrete geometric conservation law is a sufficient condition for the backward Euler implicit scheme to be unconditionally stable. This new result sheds some light on the relationship between the DGCL and numerical stability. However, it does not take into account the nonlinearities that characterize Euler flows, and stops short from predicting the behavior of an ALE scheme that does not satisfy its corresponding DGCL. For this reason, Farhat, Geuzaine and Grandmont have investigated further the theoretical status of the DGCL, and exposed its relation to *nonlinear* stability. More specifically, using a three-dimensional nonlinear scalar hyperbolic conservation law as a model problem, they have proved for sample arbitrary Lagrangian Eulerian schemes that the DGCL requirement corresponds to a necessary and sufficient condition for a numerical scheme to achieve nonlinear stability. Consequently, they have also shown that an ALE scheme which violates its DGCL is bound to exhibit spurious oscillations and overshoots for practical computational time-steps, and can occasionally exhibit an unbounded behavior. For all these reasons, and because the computational overhead associated with enforcing a DGCL is minimal — for example, whether equipped with Eqs. (17) or Eqs. (18), scheme (12) computes only one convective and one diffusive flux per time-step — we prefer numerical methods that satisfy their DGCLs. In particular, we prefer the four-point rule version (18) of the time-integrator (12) over its one-point rule version (17). Furthermore, we point out that in [16] and references cited therein, it was shown that for a specified accuracy, the four-point rule (18) allows a computational time-step that is more than an order of magnitude larger than that afforded by straightforward and geometrically non conservative extensions to moving grids of the three-point backward difference scheme. Hence, it is now well established that satisfying the governing DGCL improves significantly both robustness and

performance.

### 3.2 Energy conservative exchange of aerodynamic and elastodynamic data

Next, we turn our attention to the discretization of the transmission conditions (4,6). In order to address the practical case where the fluid and structure computational domains have non-matching discrete interfaces, we denote by  $\Gamma_F$  and  $\Gamma_S$  the discrete representations of the fluid-structure interface  $\Gamma$  on the fluid and structure sides, respectively.

The energy transferred from the fluid to the structure through  $\Gamma$  during the time-interval  $[t^n, t^{n+1}]$  is

$$\delta \mathcal{E}_F^{n+1} = - \int_{t^n}^{t^{n+1}} \left( \int_{\Gamma} (-pn + \sigma_F \cdot n) \dot{x} \, ds \right) dt \quad (19)$$

and that received by the structure during the same time-interval is

$$\delta \mathcal{E}_S^{n+1} = \int_{t^n}^{t^{n+1}} \left( \int_{\Gamma} \sigma_S \cdot n \dot{u}_S \, ds \right) dt \quad (20)$$

From the above expressions and Eqs. (4,6), it follows that the discretization of the transmission conditions (4,6) has a direct impact on the conservation of the energy transferred between the fluid and the structure through  $\Gamma$ .

Whichever approximation method (interpolation, projection, etc.) is chosen for enforcing on  $\Gamma$  the compatibility of the displacement fields of the fluid mesh and the structure (6), its outcome can be written as follows

$$x_j = \sum_{i=1}^{i_S} c_{ji} u_{S,i}^P \quad j \in \Gamma_F, i \in \Gamma_S \quad (21)$$

where  $x_j$  is the discrete value of  $x$  at the fluid point  $j$ , and  $u_{S,i}$  is the discrete value of  $u_S$  at the structure node  $i$ . The integer  $i_S$  and real coefficients  $c_{ji}$  depend on the chosen method of approximation. The superscript  $P$  is used to designate a "prediction" of the motion of the structure. If the fluid and structure subsystems are solved simultaneously,  $u_S^P = u_S$ . On the other hand, if they are advanced in time by a staggered procedure (see Section 3.3),  $u_S^P$  will in general differ from  $u_S$ , because of a time-lag between the fluid and structure partitions.

Consider now a virtual displacement field  $\hat{x}$  that is zero on each degree of freedom of the moving fluid grid except on those lying on the boundary  $\Gamma_F$ . Whichever method is chosen for approximating Eq. (3c) and therefore constructing the pseudo-structural stiffness matrix  $\tilde{K}$  (see Eq. (10)),  $\hat{x}$  can be expressed as follows

$$\hat{x} = \sum_{j=1}^{j_F} D_j \hat{x}_j \quad j \in \Gamma_F \quad (22)$$



where  $D_j$  is some function with a local or global support on  $\Gamma_F$ . From Eq. (19) and Eq. (22), it follows that the virtual work during  $[t^n, t^{n+1}]$  of the fluid tractions acting on  $\Gamma_F$  is

$$\begin{aligned}\delta W_F^{n+1} &= \int_{t^n}^{t^{n+1}} \left( \sum_{j=1}^{j_F} \int_{\Gamma_F} (-pn + \sigma_F \cdot n) D_j \dot{\hat{x}}_j ds \right) dt \\ &= \int_{t^n}^{t^{n+1}} \sum_{j=1}^{j_F} \Phi_j \dot{\hat{x}}_j dt\end{aligned}\quad (23)$$

where  $\Phi_j$  has the physical meaning of a numerical pressure flux and is given by

$$\Phi_j = \int_{\Gamma_F} (-pn + \sigma_F \cdot n) D_j ds \quad (24)$$

Substituting Eq. (21) into Eq. (23) gives

$$\delta W_F^{n+1} = \int_{t^n}^{t^{n+1}} \sum_{j=1}^{j_F} \Phi_j \dot{\hat{x}}_j dt = \sum_{i=1}^{i_S} \int_{t^n}^{t^{n+1}} f_{F_i} \dot{\hat{u}}_{S_i}^P dt \quad (25)$$

where

$$f_{F_i} = \sum_{j=1}^{j_F} [\Phi_j][c_{ji}] \quad j \in \Gamma_F, i \in \Gamma_S \quad (26)$$

If the nodal aerodynamic forces (and moments) acting on a structure node  $i$  lying on  $\Gamma_S$  are denoted by  $f_{S_i}^{ae}$ , the virtual work during  $[t^n, t^{n+1}]$  of these forces is

$$\delta W_S^{n+1} = \int_{t^n}^{t^{n+1}} \sum_{i=1}^{i_S} f_{S_i}^{ae} \dot{\hat{u}}_{S_i} dt = \sum_{i=1}^{i_S} \int_{t^n}^{t^{n+1}} f_{S_i}^{ae} \dot{\hat{u}}_{S_i} dt \quad (27)$$

Conserving the transfer of energy through  $\Gamma$  requires enforcing  $\delta W_F^{n+1} = \delta W_S^{n+1}$  for any pair of virtual displacement vectors  $\hat{x}$  and  $\hat{u}_S$  satisfying (21). From Eqs. (25,27), this implies enforcing

$$\int_{t^n}^{t^{n+1}} f_{S_i}^{ae} \dot{\hat{u}}_{S_i} dt = \int_{t^n}^{t^{n+1}} f_{F_i} \dot{\hat{u}}_{S_i}^P dt \quad (28)$$

The evaluation of the time-integrals in Eq. (28) depends on the time-integration schemes chosen for the structure and fluid analyses, and is discussed in great details in [14]. Here, we focus on the case where Eq. (8) is time-integrated with the popular midpoint rule — which is second-order time-accurate and in the linear case identical to the Newmark algorithm with  $\beta = 1/4$  and  $\gamma = 1/2$  [21] — and the flow equations (7) are time-integrated with the second-order

time-accurate extension to moving grids of the three-point backward difference scheme described by Eqs. (12,18). In that case, Eq. (28) becomes

$$\frac{f_{S_i}^{ae^{n+1}} + f_{S_i}^{ae^n}}{2} (u_{S_i}^{n+1} - u_{S_i}^n) = \frac{f_{F_i}^{n+1} + f_{F_i}^n}{2} (u_{S_i}^{n+1^P} - u_{S_i}^{n^P}) \quad (29)$$

If the fluid and structure subsystems are solved simultaneously,  $u_S^{n^P} = u_S^n$ , and Eq. (29) simplifies to

$$f_{S_i}^{ae} = f_{F_i} = \sum_{j=1}^{j_F} [\Phi_j][c_{ji}] \quad j \in \Gamma_F, i \in \Gamma_S \quad (30)$$

In that case, Eq. (30) describes a conservative algorithm for transmitting the fluid forces to the structure. This algorithm is independent of the method chosen for discretizing the structure. The term in the first bracket in Eq. (30) depends exclusively on the method chosen for discretizing the flow problem, and the term in the second bracket depends only on the method selected for transmitting the displacement of the structure to the fluid mesh.

If a time-lag is introduced in the solution of the fluid and structure subsystems,  $u_S^{n^P} \neq u_S^n$ . In that case, conserving the energy transfer through  $\Gamma$  requires subiterating on  $u_S^{n^P}$  until  $u_S^{n^P} = u_S^n$ . However, even if no subiterations are performed, we still recommend exchanging the aerodynamic data between the fluid and the structure according to Eq. (30), and discuss in Section 3.3 effective means for compensating the strict loss of conservation of energy transfer through  $\Gamma$ .

### 3.3 Higher-order loosely coupled fluid-structure time-integrators

For any reasonably detailed FE representation of the aircraft structure, the simultaneous solution of Eqs. (3) by a monolithic scheme is neither practical nor software-wise manageable. For this and other reasons related to computational efficiency, a partitioned procedure is typically employed for solving coupled field nonlinear aeroelastic problems. In such a procedure, the fluid and structure are time-integrated by different schemes tailored to their different mathematical models, and the resulting discrete equations are solved by a staggered algorithm [10, 23, 24]. Such a strategy simplifies explicit/implicit treatment, subcycling, load balancing, software modularity, and replacements as better mathematical models and methods emerge in the fluid and structure disciplines. The most popular partitioned procedure, which is referred to in this paper as the Conventional Serial Staggered (CSS) procedure, is graphically depicted in Fig. 2. Its generic cycle between  $t^n$  and  $t^{n+1}$  can be described as follows: (1) predict  $u_S^{n+1^P} = u_S^n$ , transfer the corresponding motion of the wet boundary of the structure to the fluid subsystem, and update the position of the moving fluid mesh accordingly, (2) advance the fluid subsystem to  $t^{n+1}$  using a given flow time-integrator and compute a new set of aerodynamic forces  $f_F^{n+1}$

acting on  $\Gamma_F$ , (3) transfer  $f_S^{ae^{n+1}} = f_F^{n+1}$  to the structure subsystem, (4) apply  $f_S^{ae^{n+1}}$  to the structure and advance it to  $t^{n+1}$  using a given time-integrator. Such a staggered procedure, which can be described as a loosely coupled solution algorithm, can also be equipped with a subcycling strategy where the fluid and structure subsystems are advanced using different time-steps  $\Delta t_F$  and  $\Delta t_S$ .

Unfortunately, the time-accuracy of the CSS procedure is in general at least one order lower than that of its underlying flow and structure time-integrators, and its numerical stability is more restrictive than that of the flow and structure solvers. Consequently, its maximum allowable time-step is much smaller than required for accuracy purposes, which makes it a slow algorithm. To improve the performance of this simple partitioned procedure, several ad-hoc strategies have been proposed in the literature. Essentially, these strategies insert some type of predictor/corrector iterations within each cycle of the computations in order to compensate for the time-lag between the fluid and structure solvers [23, 25, 26]. These iterations help closing the gap between  $u_S^{n+1^P}$  and  $u_S^{n+1}$ , and therefore as explained in Section 3.2 (see Eq. (29)) they also help conserving the transfer of energy between the fluid and structure through  $\Gamma$ . As a result, they increase the maximum allowable time-step of the CSS procedure. However, since the numerical complexity of each predictor/corrector iteration is almost the same as that of one cycle of staggering, little CPU is saved by such enhancement strategies.

Recently, Piperno and Farhat [14] have presented an alternative approach for improving the maximum allowable time-step of the CSS procedure that does not increase its computational cost per cycle. Their approach, which assumes that  $f_F^{n+1}$  is computed as in Eq. (26), is based on introducing two computationally economical factors for compensating the time-lag between the fluid and the structure subsystems: (1) a non-trivial prediction  $u_S^{n+1^P} \neq u_S^n$ , and (2) a non necessarily trivial transfer of the aerodynamic forces to the structure  $f_S^{ae^{n+1}} \neq f_F^{n+1}$ . More specifically, they have shown that given two time-integration schemes for the fluid and structure equations of motion,  $u_S^{n+1^P}$  and  $f_S^{ae^{n+1}}$  can be designed to achieve

$$\sum_{n=0}^{NT/\Delta t} \delta W_F^n + \delta W_S^n = O(\Delta t^p) \quad (31)$$

where  $N$  is an arbitrary integer,  $T$  is the period of an assumed harmonic vibration of the structure, and  $\Delta t = \Delta t_F = \Delta t_S$  is a fixed time-step for the fluid and structure time-integrators. In other words,  $u_S^{n+1^P}$  and  $f_S^{ae^{n+1}}$  can be designed to construct a  $p$ -order "energy-transfer-accurate" CSS procedure. The higher  $p$  is, the closer is the CSS procedure to conserving the transfer of energy through the fluid-structure interface. For example, consider the case where the CSS procedure is equipped with the midpoint rule for time-integrating the structure subsystem, and the extension to moving grids of the three-point backward difference scheme described by Eqs. (12,18) for integrating the fluid subsystem. When  $u_S^{n+1^P} = u_S^n$  and  $f_S^{ae^{n+1}} = f_F^{n+1}$ , this CSS procedure is only first-order

energy-transfer-accurate. On the other hand, if  $u_S^{n+1P}$  is predicted by the following first-order scheme

$$u_S^{n+1P} = u_S^n + \frac{\Delta t_S}{2} \dot{u}_S^n \quad (32)$$

and the following “improved” vector of aerodynamic forces is applied on the wet surface of the structure

$$f_S^{ae^{n+1}} = 2f_F^{n+1} - f_S^{ae^n} \quad (33)$$

the CSS procedure becomes third order energy-transfer-accurate and its maximum allowable time-step is increased by a factor equal to 5. This significant improvement in performance is achieved without any predictor/corrector iteration and almost at zero cost.

In [14], it is also shown that the Improved Serial Staggered (ISS) procedure proposed by Lesoinne and Farhat in [27] is also third-order energy-transfer-accurate, and allows a maximum time-step that is at least as large as that of the CSS procedure equipped with the first-order prediction (32) and the improved aerodynamic forces (33). This is not surprising because as shown in Fig. 3, the ISS procedure incorporates the effects of the improved prediction (32) and aerodynamic forces (33).

Finally, we note that the combination of the advanced fluid time-integrators highlighted in Section 3.1 and improved staggered procedures overviewed herein has improved the computational efficiency and performance of the state-of-the-art technology for the solution of nonlinear transient aeroelastic problems by a factor ranging between 10 and 22 [27].

## 4 The AERO-F/AERO-S simulation platform

The AERO-F, AERO-S, and MATCHER codes developed at the University of Colorado are a suite of software modules based on the three-field formulation described in this paper for the solution on nonlinear transient aeroelastic problems. They are portable, and run on a large variety of computing platforms ranging from Unix workstations to shared as well as distributed memory massively parallel computers.

The two- and three-dimensional AERO-F modules model a flow either by the Euler equations, or the averaged Navier-Stokes equations equipped with the  $k$ - $\epsilon$  turbulence model and a wall function. They operate on static and dynamic unstructured meshes. More specifically, they combine a Galerkin centered approximation for the viscous terms, and a Roe upwind scheme for the convective fluxes. Higher-order spatial accuracy is achieved through the use of a multidimensional piecewise linear reconstruction that follows the principle of the Monotonic Upwind Scheme for Conservative Laws [28]. Time-integration on fixed grids can be performed either by a 3-step variant of the explicit Runge-Kutta algorithm, or by the implicit three-point backward difference scheme. Time-integration on

moving grids is carried out as described in this paper. All linearized systems of equations are solved by the RAS (Restricted Additive Schwarz) preconditioned GMRES iterative algorithm [31].

The AERO-F modules support two robust structure analogy methods for constructing dynamic meshes. The first one is based on time-dependent torsional springs [29, 30]. The second method is based on the total Lagrangian approach for solving a fictitious nonlinear elasticity problem [32]. Both methods share in common the idea of constructing the fictitious stiffness of each fluid mesh element so that it increases to infinity when its area or volume decreases to zero. This prevents all collapsing mechanisms (node-to-node, node-to-edge, and node-to-face) from occurring during the mesh motion. For applications where the structure undergoes large rotations — for example, aircraft maneuvering — the AERO-F modules invoke a corotational scheme to accelerate the update of the mesh motion [33].

The AERO-S suite of structural and thermal modules are capable of linear and geometrically nonlinear static, sensitivity, vibration (eigen), and transient FE analyses of restrained as well as unrestrained homogeneous and composite structures.

The AERO-F and AERO-S suite of codes communicate via run-time software channels. They exchange aerodynamic and aeroelastic data across non-matching fluid and structure mesh interfaces as described in this paper. For that purpose, they are guided by information generated in a preprocessing phase by the MATCHER software [34].

## 5 Application to the prediction of the aeroelastic parameters of an F-16 configuration

The validation of the AERO-F, AERO-S, and MATCHER codes for the flutter analysis of the AGARD Wing 445.6 is described in [27]. For this relatively simple wing problem, these codes and the underlying algorithms described in this paper have proved to be capable of capturing correctly the transonic dip. They have also demonstrated a superior computational efficiency by operating accurately with a fluid time-step  $\Delta t_F$  that is 10 to 22 times larger, and a coupling time-step  $\Delta t = \max(\Delta t_S, \Delta t_F)$  that is 20 to 46 times larger, than reported in the literature for other nonlinear aeroelastic codes [27, 35]. Here, we validate our nonlinear transient aeroelastic simulation technology for an industrial problem in view of assessing its potential for replacing flutter testing of scaled models in transonic wind tunnels. For this purpose, we simulate the flutter clearance of an F-16 Block-40 in clean wing configuration but with tip missiles, for  $0.8 \leq M_\infty \leq 1.4$  and at the altitude of 3,000 m. For this purpose, we first represent the structural behavior of this fighter by that of its typical wing section, then by that of a detailed three-dimensional FE model. We perform all computations in double precision arithmetic on a Silicon Graphics Origin 2000 parallel computer. We contrast the results obtained using both approaches and compare them to flight

test data provided by the Flight Test Center at the Edwards Air Force Base.

### 5.1 Typical wing section model

From a structural viewpoint, a typical wing section (TWS) is characterized by two degrees of freedom (dof)  $h$  and  $\theta$  which represent the behavior of the wing in bending and torsion, respectively (see Fig. 4). It is identified by the following parameters

$$P_{TWS} = \{m, I_\theta, x_G, (x_G - x_C), K_h, K_\theta\}$$

where  $m$  is the total mass per unit span of the wing,  $x_G$  and  $x_C$  designate the center of gravity and elastic center of the TWS,  $S_\theta = m(x_G - x_C)$  and  $I_\theta$  denote its static and polar moments of inertia about the elastic axis, and  $K_h$  and  $K_\theta$  are its bending and torsional stiffness coefficients. From an aerodynamic viewpoint, a TWS has the shape of the airfoil of the wing.

In order to design a TWS for the F-16 Block 40, we start from a detailed FE structural model of a clean right wing of this fighter with a missile and its launching system at the wing tip (see Fig. 5). We determine the set of parameters  $P_{TWS}$  by requiring that the sought-after TWS be equivalent to the wing of the F-16 Block 40 in the following sense

1. It reproduces the first bending and torsion frequencies of the dry wing which are 4.76 Hz and 7.43 Hz, respectively.
2. It reproduces the same bending and torsion modal masses.
3. It reproduces the same vertical displacement at the leading edge of the cross section located at 68% of the distance from the root to the tip of the wing, for both bending and torsion mode shapes, when these are normalized to a unit rotation of the cross section.

For criterion 3, we choose the wing cross-section located at 68% of the distance from the root to the tip (see Fig. 5) because the F-16 wing is strongly tapered and is rather soft towards its tip. The criteria stated above lead to

$$\begin{aligned} m &= 2.05 \cdot 10^3 \text{ Kg} \\ I_\theta &= 2.53 \cdot 10^3 \text{ Kg.m}^2 \\ x_G &= 1.126 \text{ m (upstream of section at 68\%)} \\ (x_G - x_C) &= 0.0642 \text{ m (G behind C)} \\ K_h &= 2.046 \cdot 10^6 \text{ N/m} \\ K_\theta &= 5.468 \cdot 10^6 \text{ N.m} \end{aligned}$$

We choose the shape of the typical wing section as that of the airfoil located at 45% of the distance between the root and tip of the F-16 wing (see Fig. 5). This choice is justified by two factors: (a) the chord of the airfoil of the TWS must be close to the ratio of the wetted area and the wing span, and (b) because



of tapering, most of the lift is generated by the section of the wing that is close to the root, which implies that the aerodynamic center of the wing is within this area. We discretize the two-dimensional flow domain by 18,000 vertices, and ensure a sufficient resolution for shock capturing in the region close to the thin leading edge (see Fig. 6).

## 5.2 Detailed FE model

Based on modeling information provided by Lockheed-Martin, we construct a detailed three-dimensional FE structural *dynamics* model of the F-16 Block 40 in clean wing configuration with a missile and launching system at each wing tip. This FE model features bar, beam, solid, plate, shell, metallic as well as composite elements, and a total of 168,799 dofs (see Fig. 7(a)). Like the TWS, this FE model reproduces correctly the first dry bending and torsion frequencies measured to be 4.76 Hz and 7.43 Hz, respectively. Using the Gridgen™ software and F-16 CAD data provided by the Air Force Research Laboratory at Wright Patterson, we ignore the wing tip missiles and generate first a surface grid with 63,044 grid points (see Fig. 7(b)). Then, we generate a fluid volume mesh with 403,919 vertices.

## 5.3 Parameter identification

Let  $\bar{f}_{ben}$  ( $\bar{f}_{tor}$ ) and  $\bar{\alpha}_{ben}$  ( $\bar{\alpha}_{tor}$ ) denote respectively the frequency (in Hz) and damping coefficient of the first aeroelastic mode of the F-16 configuration considered herein that is dominated by bending (torsion). To determine these aeroelastic parameters, we mimic the procedure employed in flight testing. Whether using the TWS or detailed FE model, we excite the structure in an appropriate manner and simulate numerically its response to the prescribed initial disturbance. In the case of the TWS model, the numerical simulation generates two signals:  $h(t)$  and  $\theta(t)$ . In the case of the detailed FE model, it generates 168,799 signals, one for each dof of this model. Hence, in the latter case, we focus only on the vertical displacement dofs at one tip node and one root node of each wing. This corresponds to positioning output sensors at these locations for flight testing. Once the signals are generated for a sufficiently long period of time, we apply the Eigensystem Realization Algorithm (ERA) [36] to extract from them the aeroelastic parameters  $\bar{f}_{ben}$ ,  $\bar{f}_{tor}$ ,  $\bar{\alpha}_{ben}$ , and  $\bar{\alpha}_{tor}$ .

The ERA is a real-time parameter identification method that is less sensitive to noise than the classical logarithmic decay method. It can handle multi-input multi-output (multi-dof) systems. Most importantly, it is capable of identifying the frequencies and damping coefficients of the two lowest dominating modes of a structure using as few as 2 cycles of response history, as long as the sampling rate is on the order of 500 to 1000 Hz ( $\Delta t = 1$  to 2 milliseconds) [37]. Hence, it is particularly attractive to time-domain aeroelastic applications as it requires the simulation of only two cycles of the vibration of the structure.

## 5.4 Validation

We have chosen the F-16 configuration described in this paper because it is the only configuration for which we were able to obtain modeling information. However, the only F-16 flight test data we were successful in obtaining is for the aeroelastic torsional mode of a Block 40 configuration flying at the same altitude of 3,000 m, but equipped with 3 launchers, 2 pylons, and one missile (close to the tip) under each wing. Hence, at least because of these differences in wing configurations, some discrepancy is to be expected between the results predicted by our simulations for  $0.8 \leq M_\infty \leq 1.4$  (for example, see Fig. 8) and the available flight test data.

The results reported in Figs. 9-10 show that

- The aeroelastic bending frequencies predicted using the TWS model differ from those predicted using the detailed three-dimensional FE model by less than 5%. For the aeroelastic torsional mode, the maximum relative difference is 12.5% and occurs around  $M_\infty = 1$ .
- The aeroelastic torsional frequencies predicted using both structural models correlate reasonably well with flight test results. Those predicted using the detailed three-dimensional FE model are however more accurate: depending on the Mach number, they either agree very well with the aeroelastic torsional frequencies measured during flight test or differ at most by 7%.
- The aeroelastic damping coefficients of the torsional mode computed using the TWS model do not correlate well with flight test data. They erroneously predict flutter for  $0.9 \leq M_\infty \leq 1.4$ .
- The aeroelastic damping coefficients of the torsional mode obtained using the detailed three-dimensional FE model correlate reasonably well with flight test data. In particular, they reproduce the same trend of variation with the Mach number.

It follows that while the TWS model offers obvious practical and computational advantages that make it popular — at least in the research community — for flutter analysis, it does not appear to be reliable for fighter applications. This is partly because the TWS model is realistic only for fairly homogeneous wings with high aspect ratios and small angles of sweep. However, the results reported herein also show that when applied to three-dimensional structural and fluid models, our nonlinear aeroelastic simulation capability predicts well the aeroelastic parameters of the chosen F-16 configuration, including in the transonic regime.

## 5.5 Performance results

Finally, we briefly discuss the speed of the nonlinear aeroelastic simulation technology described in this paper, particularly in the context of this second quote

from [6]: *"Even at present, existing CFD codes should be able to obtain five flutter solutions in one year."* For this purpose, we focus on the more interesting case of the detailed FE model of the F-16 fighter with 168,799 dofs.

First, we remind the reader that we need to predict only the first two cycles of the response of the structure to an initial disturbance (see Section 5.3). For the F-16 configuration considered herein, our numerical algorithms sustain a coupling time-step on the order of 1 millisecond. This time-step corresponds to sampling the period of the first dry torsional mode of this fighter with 134 points. It also turns out that this time-step is such that 271 time-steps are needed to simulate the first two cycles of the structural response. Second, we note that we assume a linear behavior of the structure (see Eq. (9)), which is justified for flutter clearance applications in level flight.

We report in Table 1 the performance results obtained on an Origin 2000 computer equipped with R10000 195 MHz chips, as a function of the number of processors  $N_{proc}$  allocated to the simulation. These results correspond to a single Mach number point, and two cycles of the response of the structure. In all cases, we assign a single processor to the structure solver because it is less computationally intensive than the flow and mesh motion solvers. We observe that on average, 60% of the total CPU time is elapsed in the flow solver, 38% in the mesh motion solver, and only 2% in the structure solver. The small percentage of the total CPU time consumed by the structure solver is due to the assumed linear nature of the structural problem. (We note however that for maneuvering applications where nonlinear geometric effects must be accounted for, the percentage of the total CPU time elapsed in structural computations is on the order of 15%).

The parallel speed-up and parallel efficiency results reported in Table 1 highlight the good parallel scalability of our three-field based nonlinear aeroelastic simulation technology. One can reasonably argue that today, most aerospace engineers have access to a 6-processor computational platform. From the results reported in Table 1, we conclude that using such a computing system, the transonic aeroelastic parameters of a full fighter configuration can be extracted in 12.8 hours. For a given Mach number, finding the flutter speed usually requires a bracketing procedure. It is our experience that such a bracketing procedure typically incurs 4 to 5 simulations that are similar to the one discussed herein. Hence, for a given Mach number, it is also our experience that extracting the flutter speed requires between 51 and 64 hours CPU on a 6-processor computational platform. Therefore, using the AERO-F, AERO-S, and MATCHER suite of codes on a 6-processor configuration, we can obtain five flutter point solutions for a fighter in the transonic regime in less than 2 weeks. Using 24 processors for this purpose reduces the total simulation time to less than 4 days. These estimates, which do not include the time needed for building the FE structural model and generating the fluid grid, are also confirmed by our experience with the F-16 Block 40 aircraft.

## 6 Conclusions

High performance military aircraft are usually flutter critical in the transonic regime where the linear flow theory fails to predict correctly the unsteady aerodynamic forces acting on an aircraft. Consequently, flutter testing of scaled models in transonic wind tunnels is always used to generate corrections to flutter speeds predicted by linear methods. Because the design of a wind tunnel flutter model and the analysis of the corresponding data require over a year's time, it has been suggested that computational fluid dynamics (CFD) based nonlinear aeroelastic simulations could be used as a replacement for wind tunnel testing, if they prove to be practical — that is, fast enough — and reliable [6]. We believe that the nonlinear aeroelastic simulation methodology presented in this paper, as well as other similar capabilities developed elsewhere, are today sufficiently mature to take on this challenge. At the present time, they may not be sufficiently fast to be used as a design tool. However, on a 6-processor computing platform, our nonlinear aeroelastic simulation technology is capable of computing five flutter point solutions for a fighter in the transonic regime in less than 2 weeks. On a 128-processor system, it can complete the same job in less than a day. In general, nonlinear solution methodologies such as the one overviewed in this paper do not target flutter problems in the subsonic and supersonic regimes where simpler linear methods appear to satisfy industry. They are rather meant to address those nonlinear aeroelastic problems which simply cannot be tackled by the linear theory of aeroelasticity. These include, among others, flutter at transonic speeds, buffeting, and prediction of transient loads and stresses during aggressive maneuvering. The nonlinear aeroelastic simulation capability described in this paper has tremendously benefited from the technical interaction with the Flight Test Center at the Edwards Air Force Base, and its application to F-16 problems. Similar interactions with industry should accelerate its transformation into a "production" tool.

## Acknowledgments

The authors acknowledge the support by the Air Force Office of Scientific Research under Grant F49620-99-1-0037 and Grant F49620-99-1-0007. They also thank Tracy Redd, Maj. Paul Waters, and Chuck Harris from the Flight Test Center at the Edwards Air Force Base for providing them the F-16 flight test data.

## References

- [1] Farhat C. High performance simulation of coupled nonlinear transient aeroelastic problems. AGARD Report R-807, Special Course on Parallel Computing in CFD (l'Aérodynamique numérique et le calcul en parallèle), North Atlantic Treaty Organization (NATO), October 1995.

- [2] Dat R, Meurzec J L. Sur les calculs de flottement par la method dite du "balayage" en frequence reduite, La Recherche Aerospatiale 133, Nov. Dec. 1969.
- [3] Hassig H J. An approximate true damping solution of the flutter equation by determinant iteration, J. Aircraft 1971;8:885-889.
- [4] Albano E, Rodden W P. A doublet-lattice method for calculating lift distribution on oscillating surfaces in subsonic flow, AIAA J. 1969;7:279-285.
- [5] Ashley H, Zartarian G. Piston theory - A new aerodynamic tool for the aeroelastician, J. Aero. Sc. 1956;23:1109-1118.
- [6] Yurkovich R N, Liu DD, Chen P C. The state-of-the-art of unsteady aerodynamics for high performance aircraft, AIAA Paper No. 2001-0428, 39th AIAA Aerospace Sciences Meeting & Exhibit, 8-11 January 2001, Reno, NV.
- [7] Lesoinne M, Farhat C. Stability analysis of dynamic meshes for transient aeroelastic computations, AIAA Paper No. 93-3325, 11th AIAA Computational Fluid Dynamics Conference, 6-9 July 1993, Orlando, FL.
- [8] Donea J. An arbitrary Lagrangian-Eulerian finite element method for transient fluid-structure interactions, Comput. Meths. Appl. Mech. Engrg. 1982;33:689-723.
- [9] Batina J T. Unsteady Euler airfoil solutions using unstructured dynamic meshes, AIAA Paper No. 89-0115, AIAA 27th Aerospace Sciences Meeting & Exhibit, 9-12 January 1989, Reno, NV.
- [10] Farhat C, Lesoinne M, Maman N. Mixed explicit/implicit time integration of coupled aeroelastic problems: three-field formulation, geometric conservation and distributed solution, Internat. J. Numer. Meths. Fluids 1995;21:807-835.
- [11] Lesoinne M, Farhat C. Geometric conservation laws for aeroelastic computations using unstructured dynamic meshes, AIAA Paper No. 95-1709, 12th AIAA Computational Fluid Dynamics Conference, 19-22 June 1995, San Diego, CA.
- [12] Lesoinne M, Farhat C. Geometric conservation laws for flow problems with moving boundaries and deformable meshes and their impact on aeroelastic computations, Comput. Meths. Appl. Mech. Engrg. 1996;134:71-90.
- [13] Koobus B, Farhat C. Second-order time-accurate and geometrically conservative implicit schemes for flow computations on unstructured dynamic meshes, Comput. Meths. Appl. Mech. Engrg. 1999;170:103-130.
- [14] Piperno S, Farhat C. Partitioned procedures for the transient solution of coupled aeroelastic problems - Part II: energy transfer analysis and three-dimensional applications, Comput. Meths. Appl. Mech. Engrg. (in press).

- [15] Guillard H, Farhat C. On the significance of the GCL for flow computations on moving meshes, AIAA Paper No. 99-0793, 37th Aerospace Sciences Meeting & Exhibit, 11-14 January 1999, Reno, NV.
- [16] Guillard H, Farhat C. On the significance of the geometric conservation law for flow computations on moving meshes, *Comput. Meths. Appl. Mech. Engrg.* (in press).
- [17] Thomas P. D., Lombard C. K., Geometric conservation law and its application to flow computations on moving grids, *AIAA J.* 1979;17:1030-1037.
- [18] NKonga B., Guillard H. Godunov type method on non-structured meshes for three-dimensional moving boundary problems, *Comp. Meths. Appl. Mech. Engrg.* 1994;113:183-204.
- [19] Morton S A, Melville R. B., Visbal M. R. Accuracy and coupling issues of aeroelastic Navier-Stokes solutions of deforming meshes, AIAA Paper No. 97-1085, 38th AIAA Structures, Structural Dynamics and Materials Conference, 7-10 April 1997, Kissimmee, FL.
- [20] Formaggia L., Nobile F. A stability analysis for the arbitrary Lagrangian Eulerian formulation with finite elements, *East-West J. Numer. Math.* 1999;7:105-131.
- [21] Hughes T J R. Analysis of transient algorithms with particular reference to stability behavior, in: T. Belytschko and T. J. R. Hughes, ed., *Computational Methods for Transient Analysis* 1983:67-155.
- [22] Koobus B., Farhat C. On the implicit time-integration of semidiscrete viscous fluxes on unstructured dynamic meshes, *Internat. J. Numer. Meths. Fluids* 1999;29(8):975-996.
- [23] Strganac T W, Mook D T. Numerical model of unsteady subsonic aeroelastic behavior, *AIAA J.* 1990;28:903-909.
- [24] Gupta K K. Development of a finite element aeroelastic analysis capability, *J. Aircraft* 1996;33:995-1002.
- [25] Pramono E, Weeratunga S K. Aeroelastic computations for wings through direct coupling on distributed-memory MIMD parallel computers, AIAA Paper No. 94-0095, 32nd Aerospace Sciences Meeting & Exhibit, Reno, 10-13 January 1994, Reno, NV.
- [26] Mouro J. Numerical simulation of nonlinear fluid structure interactions problems and application to hydraulic shock-absorbers, *Proc. Third World Conf. Appl. Computational Fluid Dynamics, Basel World User Days CFD*, 19-23 May 1996.
- [27] Farhat C, Lesoinne M. A higher-order subiteration free staggered algorithm for nonlinear transient aeroelastic problems, *AIAA J.* 1998;36(9):1754-1756.



- [28] Dervieux A. Steady Euler simulations using unstructured meshes, Von Kármán Institute Lecture Series, 1985.
- [29] Farhat C, Degand C, Koobus B, Lesoinne M. Torsional springs for two-dimensional dynamic unstructured fluid meshes, *Comput. Meths. Appl. Mech. Engrg.* 1998;163:231-245.
- [30] Koobus B, Tran H, Farhat C. Computation of unsteady viscous flows around moving bodies using the  $k-\varepsilon$  turbulence model on unstructured dynamic grids, *Comput. Meths. Appl. Mech. Engrg.* 2000;190:1441-1466.
- [31] Cai X C, Farhat C, Sarkis M. A minimum overlap restricted additive Schwarz preconditioner and applications in 3D flow simulations, *Contemporary Mathematics* 1998;218:478-484.
- [32] Lesoinne M, Lieu T. A Geometrically non-linear mesh motion technique for large displacements of unstructured fluid meshes for aeroelastic simulations, *Proceedings ECCM-2001 Conference, Poland.*
- [33] Farhat C, Pierson K, Degand C. A CFD based simulation of the unsteady aeroelastic response of a maneuvering vehicle, *Proceedings of the European Congress on Computational Methods in Applied Sciences and Engineering (ECCOMAS), 11-14 September 2000, Barcelona, Spain.*
- [34] Maman N, Farhat C. Matching fluid and structure meshes for aeroelastic computations: a parallel approach, *Comput. & Struc.* 1995;54(4):779-785.
- [35] Farhat C, Lesoinne M. Two efficient staggered procedures for the serial and parallel solution of three-dimensional nonlinear transient aeroelastic problems, *Comput. Meths. Appl. Mech. Engrg.* 2000;182:499-516.
- [36] Juang J N, Pappa R S. An eigensystem realization algorithm (ERA) for modal parameter identification and model reduction, *J. of Guidance, Control, and Dynamics* 1985;8:620-627.
- [37] Farhat C, Harris C, Rixen D. Expanding a flutter envelope using accelerated flight data: application to an F-16 fighter configuration, *AIAA Paper No. 2000-1702, 41st AIAA/ASME/ASCE/AHS/ASC Structures, Structural Dynamics, and Materials Conference, 3-6 April 2000, Atlanta, GA.*

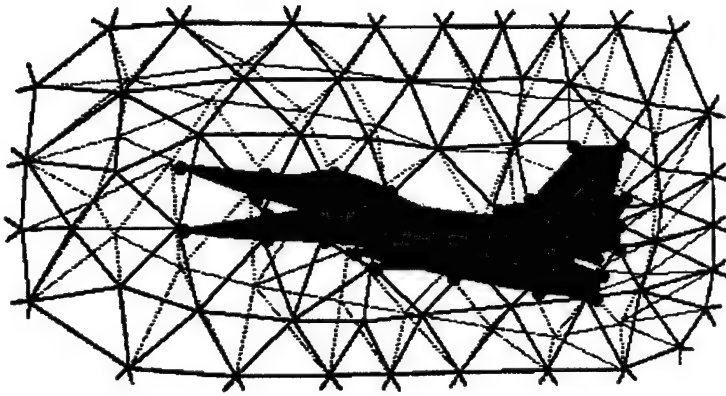


**Figure 1:** Unstructured moving fluid grid

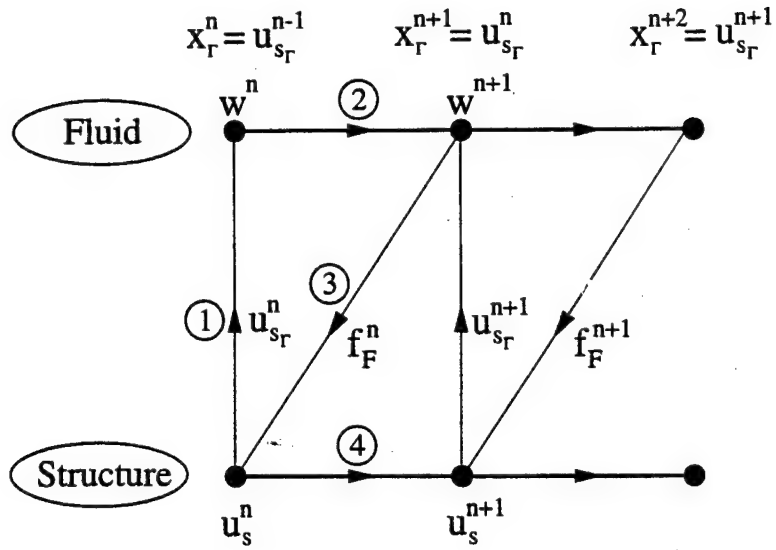


Figure 2: CSS: the conventional serial staggered procedure

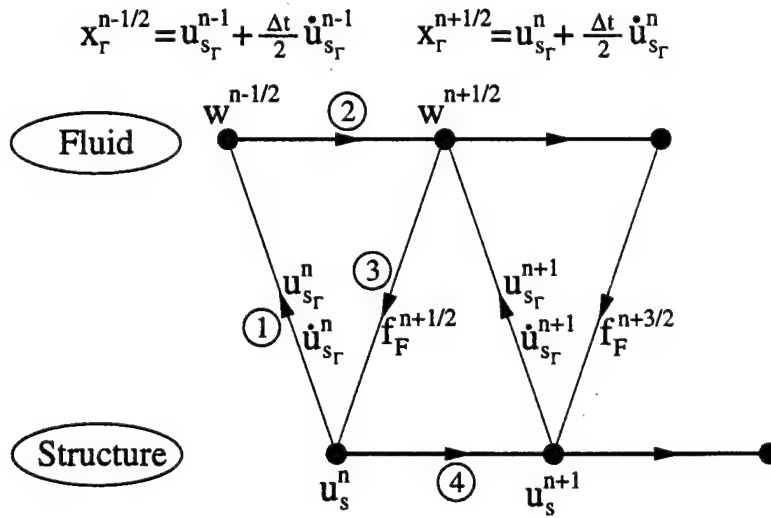
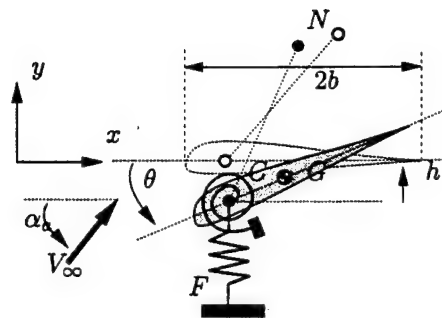
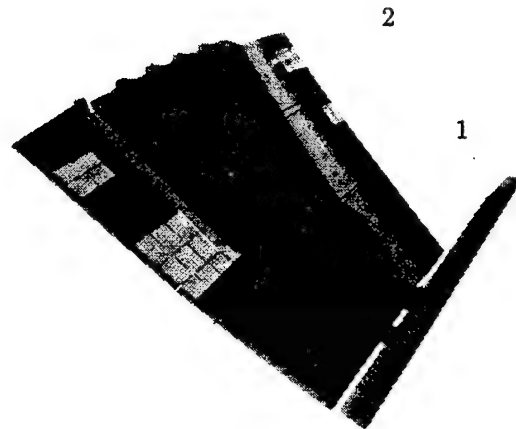


Figure 3: ISS: the improved serial staggered procedure



**Figure 4:** A typical wing section: elastic center (C), center of gravity (G), fuselage (F), angle of attack ( $\alpha_a$ ), free-stream velocity ( $V_\infty$ ), a typical point in the flow domain (N)



1: cross-section chosen for identifying the structural properties  
2: cross-section chosen for identifying the aerodynamic properties

**Figure 5:** FE model of the right wing of an F-16 Block 40

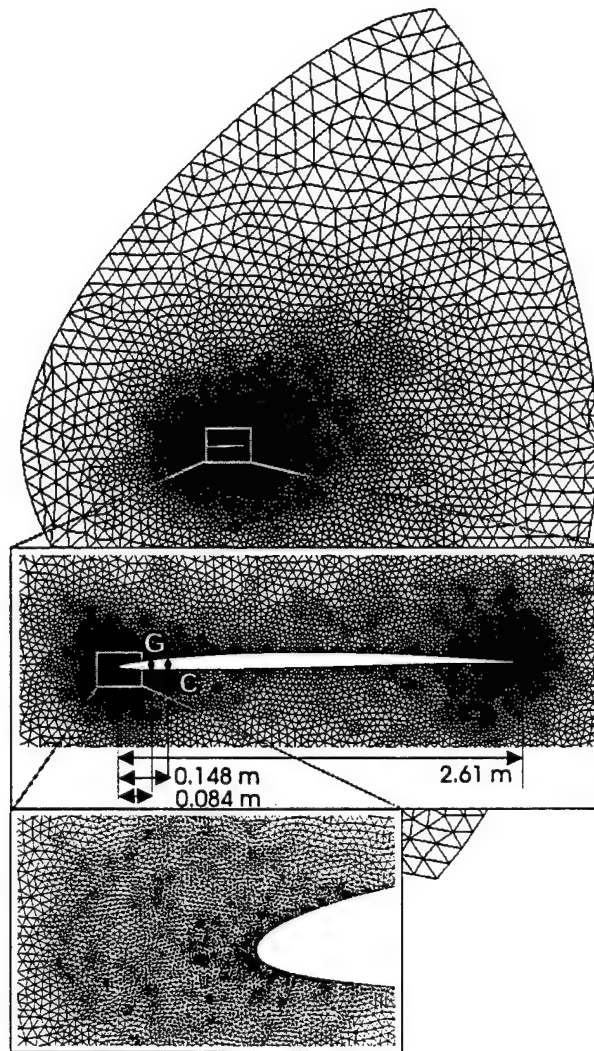
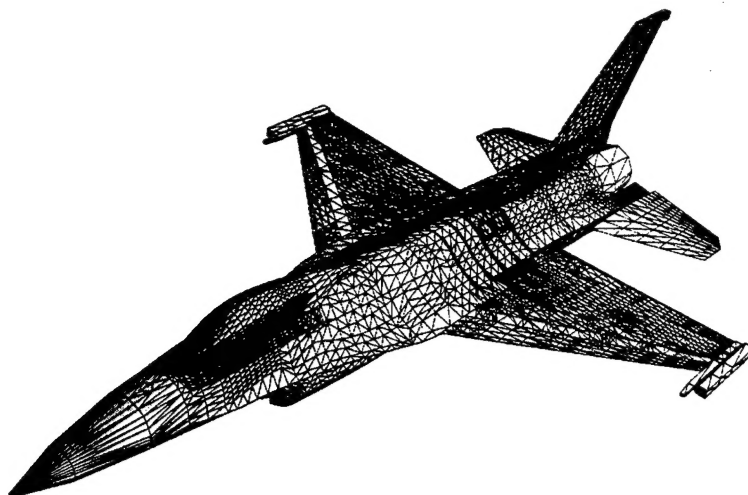
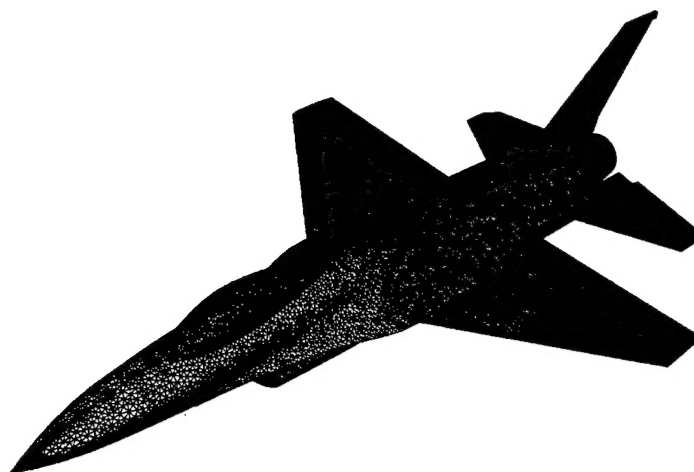


**Figure 6:** Discretization of the flow domain around an F-16 airfoil



(a) Detailed FE structural model



(b) Fluid surface grid

**Figure 7:** CSM and CFD models for an F-16 Block 40



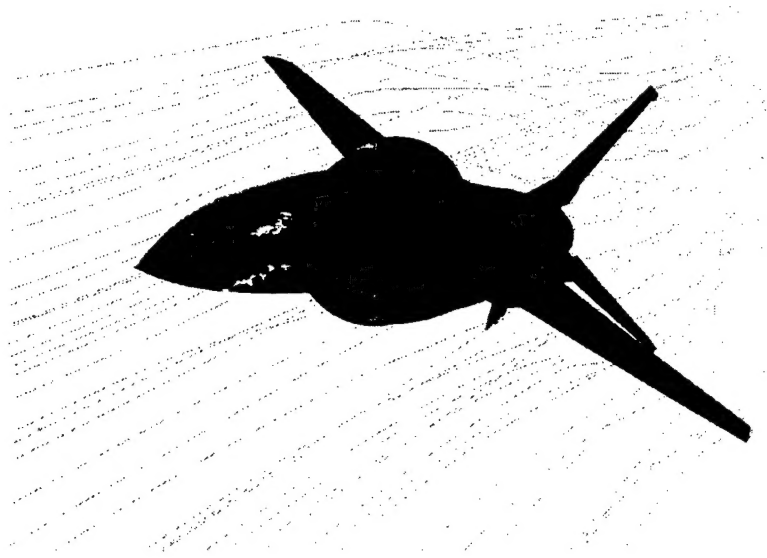


Figure 8: Mach contours and streamlines for an F-16 Block 40 at  $M_\infty = 0.9$

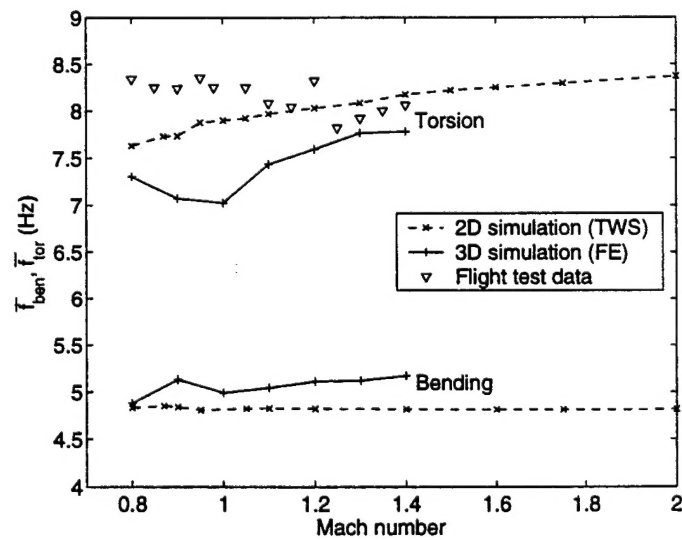
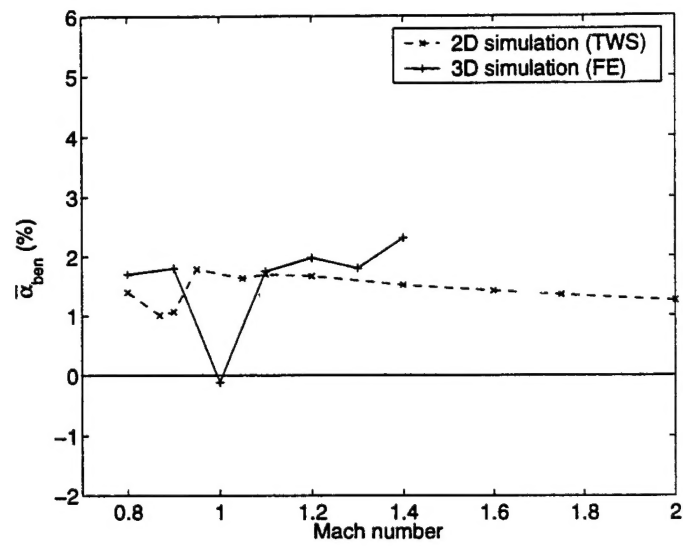
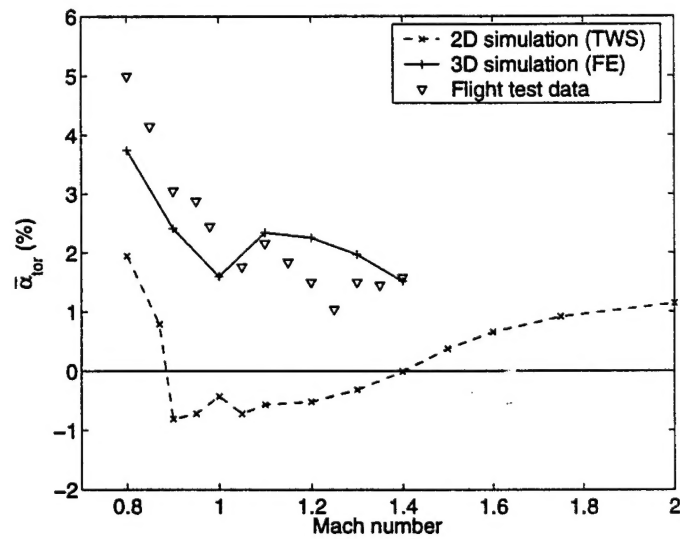


Figure 9: F-16 Block 40: aeroelastic frequencies at an altitude of 3,000 m



(a) Bending Mode



(b) Torsion Mode

**Figure 10:** F-16 Block 40: aeroelastic damping coefficients at an altitude of 3,000 m

$N_{proc}$	CPU Total	CPU Fluid	CPU Mesh	CPU Structure	Parallel Speed-up	Parallel Efficiency
1	69.8 hrs	62.4 %	37.4 %	0.2 %	1.0	100 %
3	24.6 hrs	64.6 %	34.8 %	0.6 %	2.8	95 %
6	12.8 hrs	63.3 %	35.4 %	1.3 %	5.4	91 %
12	5.9 hrs	57.1 %	40.1 %	2.8 %	11.9	99 %
24	3.3 hrs	52.7 %	42.7 %	4.6 %	20.9	87 %

**Table 1:** F-16 flutter clearance: Euler flow model with 403,919 grid points, FE structural model with 168,799 dofs — Performance results on an Origin 2000 for a single Mach number point and two cycles of the response of the structure (271 coupling time-steps)